Enhanced monoamine metabolism in lymphangioleiomyomatosis identifies plasma biomarkers and therapeutic opportunities

Carmen Herranz[1], Francesca Mateo[1], Gorka Ruiz de Garibay[1], Alexandra Junza[2], Nadia García[1], Álvaro Casanova[3], Jordi Capellades[2], Simon R. Johnson[4], Suzanne Miller[4], Antonio Gómez[5], Luis Palomero[1], Alexandra Baiges[1], Roderic Espín[1], Eva Revilla-López[6], María Molina-Molina[7], Ana Montes-Worboys[7], Carlos Machahua[7], Javier A. Menendez[1], Ana I. Extremera[1], Josep M. Cruzado[8], Roser Guiteras[8], Christophe Bontoux[9], Concettina La Motta[10], Aleix Noguera-Castells[11], Mario Mancino[11], Enrique Lastra[12], José A. Rodríguez-Portal[13], Jose C. Perales[14], Francesc Viñals[1,14], Alvaro Lahiguera[1], Xiaohu Zhang[15], Claudia Valenzuela[16], Tamara Alonso[16], Piedad Ussetti[17], Rosalía Laporta[17], Antoni Xaubet[18†], Julio Ancochea[16], Coline H.M. van Moorsel[19], Joanne J. van der Vis[19], Marian J.R. Quanjel[19], Harilaos Filippakis[20], Razq Hakem[21], Aslihan Ugun-Klusek[22], Ellen Billett[22], Chiara Gorrini[23], Marc Ferrer[15], Antonio Roman[6], Oscar Yanes[2] & Miquel A. Pujana[1,21]

[1]ProCURE, Catalan Institute of Oncology, Oncobell, Bellvitge Institute for Biomedical Research (IDIBELL), L'Hospitalet del Llobregat, Barcelona 08908, Catalonia, Spain.
[2]Department of Electronic Engineering, IISPV, Universitat Rovira i Virgili, Tarragona 43007, and CIBER of Diabetes and Associated Metabolic Diseases (CIBERDEM), Madrid 28029, Spain.
[3]Neumology Service, University Hospital of Henares, University Francisco de Vitoria, Coslada, Madrid 28822, Spain.
[4]National Centre for Lymphangioleiomyomatosis, Nottingham University Hospitals NHS Trust, Nottinghamshire, and Division of Respiratory Medicine, University of Nottingham, Nottingham NG7 2UH, UK.
[5]Centre for Genomic Regulation (CRG), Barcelona Institute of Science and Technology, Barcelona 08003, Catalonia, Spain.
[6]Lung Transplant Unit, Neumology Service, Lymphangioleiomyomatosis Clinic, Vall d'Hebron University Hospital, Barcelona 08035, Spain.
[7]Interstitial Lung Disease Unit, Department of Respiratory Medicine, University Hospital of Bellvitge, IDIBELL, L'Hospitalet del Llobregat, Barcelona 08908, and CIBER of Respiratory Diseases (CIBERES), Madrid 28029, Spain.
[8]Experimental Nephrology, Department of Clinical Sciences, University of Barcelona, Department of Nephrology, University Hospital of Bellvitge, IDIBELL, L'Hospitalet del Llobregat, Barcelona 08908, Spain.
[9]Department of Pathology, University Hospital Pitié-Salpêtrière, Faculty of Medicine, University of Sorbonne, Paris 75006, France.
[10]Department of Pharmacy, University of Pisa, Pisa 56126, Italy.
[11]Biomedical Research Institute "August Pi i Sunyer" (IDIBAPS), Department of Medicine, University of Barcelona, Barcelona 08036, Spain.
[12]Genetic Counseling Unit, Department of Medical Oncology, University Hospital of Burgos, Burgos 09006, Spain.

[13]Medical-Surgical Unit of Respiratory Diseases, University Hospital Virgen del Rocío, Institute of Biomedicine of Seville (IBiS), Sevilla 41013, and CIBER of Rare Diseases (CIBERES), Madrid 28029, Spain.
[14]Department of Physiological Science II, University of Barcelona, Barcelona 08908, Spain.
[15]National Center for Advancing Translational Sciences (NCATS), National Institute of Health (NIH), Bethesda, MD 20892-3370, USA.
[16]Neumology Service, La Princesa Research Institute, University Hospital La Princesa, Madrid 28006, Spain.
[17]Neumology Service, University Hospital Clínica Puerta del Hierro, Majadahonda, Madrid 28222, Spain.
[18]Neumology Service, Hospital Clínic de Barcelona, Barcelona 08036, Spain.
[19]ILD Center of Excellence, St. Antonius Hospital, Nieuwegein 3435CM, The Netherlands.
[20]Pulmonary and Critical Care Medicine, Department of Medicine, Brigham and Women's Hospital and Harvard Medical School, Boston, MA 02115, USA.
[21]Princess Margaret Cancer Centre, University Health Network and Department of Medical Biophysics, University of Toronto, Toronto, Ontario M5G 2C1, Canada.
[22]School of Science and Technology, Nottingham Trent University, Nottingham NG11 8NS, UK.
[23]Princess Margaret Hospital, The Campbell Family Institute for Breast Cancer Research, Ontario Cancer Institute, University Health Network, Toronto, Ontario M5G 2C1, Canada.

[†]Deceased

Correspondence and requests for materials should be addressed to M.A.P. (email: mapujana@iconcologia.net)

Inhibition of the mechanistic target of rapamycin (mTOR) is the standard of care for lymphangioleiomyomatosis (LAM). However, this therapy has variable tolerability and some patients show progressive decline of lung function despite treatment, leading to the need for organ transplantation. LAM diagnosis and monitoring can also be challenging due to the heterogeneity of symptoms and insufficiency of non-invasive tests. Here, using a cross-disease approach, we identify LAM plasma metabolite biomarkers that, in turn, provide preclinical evidence for novel beneficial therapeutic approaches in monotherapy or in combination with rapamycin. The biomarkers are the result of enhanced metabolism of monoamines. The major histamine-derived metabolite methylimidazoleacetic acid (MIAA) is generally more abundant in LAM plasma than in samples from healthy women or patients suffering from related pulmonary diseases, and MIAA values are independent of the canonical biomarker VEGF-D. LAM tumorigenesis in immunodeficient and immunocompetent mouse models is reduced using drugs (as single agents or combined with rapamycin) approved for the treatment of other human diseases and targeting histamine receptor 1 (HRH1; loratadine), monoamine oxidase A (MAO-A; clorgyline), and MAO-B (rasagiline). Mechanistically, therapeutic responses are associated with alteration of monoamine metabolism and SRC signaling, autophagy, mitochondria homeostasis, and disease cell phenotype. This study provides fundamental insight into LAM biology, and evidence for potentially improving diagnosis and therapeutic management of patients.

Introduction

LAM is a rare neoplastic disease primarily affecting women of childbearing age and is characterized by cystic lung destruction[1,2]. LAM is typically caused by the proliferation of estrogen receptor α (ER α)-positive and progesterone receptor (PR)-positive smooth muscle-like cells with lung metastatic potential[3,4]. In sporadic LAM patients, disease cells generally carry loss-of-function mutations in the tumor-suppressor tuberous sclerosis complex 2 (*TSC2*) gene[5,6,7], which results in abnormal activation of mTOR complex 1 (mTORC1) signaling[8,9]. Germline mutations in this gene or in *TSC1* cause the multisystem disease TSC, and women with this condition may also develop LAM[1,2].

The diagnosis of LAM is challenging because of the variability of its clinical symptoms and its relative similarity to other interstitial lung pathologies. Reliable diagnosis is generally achieved when patients present with defined lung cysts and other clear manifestations, particularly renal angiomyolipomas (AMLs)[10,11]. In this context, the Multicenter International Lymphangioleiomyomatosis Efficacy and Safety of Sirolimus (MILES) clinical trial highlighted the value of measuring basal serum levels of VEGF-D to provide differential diagnoses of LAM[12,13]. This biomarker has been clinically implemented in several centers and can circumvent the need for a lung biopsy for diagnosis in some cases. However, a relatively low VEGF-D level does not rule out a diagnosis of LAM and, therefore, for patients who do not show the most typical symptoms, a lung biopsy may still be required[10,11]. In addition, basal levels of VEGF-D may fluctuate due to unknown individual factors, and its overabundance may be primarily linked to specific pathological features, mainly lymphatic abnormalities[10,14]. Therefore, complementary biomarkers may help consolidate

non-invasive differential diagnostic protocols, while providing further insight into LAM biology.

The MILES trial was a remarkable success in that it demonstrated that the use of rapamycin, an allosteric mTOR inhibitor also known as sirolimus, is beneficial for treating LAM[12]. This therapy significantly stabilizes pulmonary function and decreases AML size in most cases[15], establishing the current standard of care for the disease. However, this treatment does not fully eradicate LAM cells and, although mTOR inhibition has the drawback of immunosuppression, discontinuation of treatment generally leads to disease reversion[12,15]. In addition, a substantive fraction of patients treated with rapamycin show continued decline of lung function[16,17,18]. Therefore, much effort is directed to identify therapies that, as single agents or in combination with a reduced rapamycin dose, can improve disease care by providing complementary therapeutic options. Here, using a cross-disease approach, we identify novel LAM plasma biomarkers that, in turn, have led to the preclinical demonstration of novel beneficial therapeutic approaches in monotherapy or combined with rapamycin. A valuable biomarker is derived from the metabolism of histamine and it is independent of VEGF-D. The novel therapies are based on drugs approved for other human conditions. These results derive from the fundamental observation of enhanced monoamine metabolism in LAM.

Results

Inference from breast cancer metastatic profiles leads to the identification of novel LAM plasma metabolite biomarkers

Abnormally enhanced mTORC1 activity and expression of lung metastasis mediators are molecular features shared by lung-metastatic breast cancer and LAM[19,20]. Following on from this link, we analyzed gene expression profiles of this breast cancer type in pursuance of predictions for active LAM metabolic pathways and, as a consequence, potential plasma biomarkers. Identification of biomarkers may, in turn, uncover novel therapeutic opportunities for the disease (**Fig. 1a**). Low *TSC2* expression in breast tumors is associated with lung metastatic potential[20,21,22]; thus, we identified genes with a significant negative correlation with *TSC2* (Pearson's correlation coefficient (PCC) < 0 and one-tailed $P < 0.05$) and, among them, selected those coding for enzymes ($n = 30$) that could point to specific metabolites in plasma (**Supplementary Table S1a**). Then, enrichment analysis predicted several active metabolic pathways, some of which had previously been linked to LAM, such as mitochondrial β-oxidation and the pentose phosphate pathway (**Fig. 1b**)[23,24,25,26].

Absolute quantification assays using liquid chromatography (LC) combined with mass spectrometry (MS; LC-MS/MS) were performed for seven selected metabolites (**Supplementary Table S1b**) in plasma samples obtained from 22 LAM patients and three healthy pre-menopausal women. Four metabolites showed a trend towards over-abundance in LAM samples (Mann-Whitney test P values < 0.05) and were subsequently analyzed in plasma from an additional cohort of 30 LAM patients, 12 healthy controls, as well as samples from women with LAM-related pulmonary diseases; comprising 10 individuals

diagnosed with Langerhans cell histiocytosis, 10 with Sjögren syndrome, 7 with emphysema, and 3 with lupus erythematosus. This profiling identified a significantly greater abundance of methylimidazoleacetic acid (MIAA) in LAM plasma than in any other group (**Fig. 1c**). Notably, the levels of MIAA were not positively correlated with those of VEGF-D in LAM plasma (**Fig. 1d**), but were significantly more abundant in patients that were not receiving rapamycin treatment relative to other LAM cases (**Fig. 1e**).

The three additional metabolites tested in the validation assays (homovanillic acid (HVA), 4-hydroxyphenylacetic acid (4-HPA), and 3-methoxy-4-hydroxymandelic acid (VMA)) also showed significant differences among the sample groups, although to a lesser extent than that observed with MIAA. All three were found to be more abundant in LAM than in healthy plasma, and HVA was also more abundant in LAM plasma than in related pulmonary diseases (**Fig. 1f**). Stepwise model analysis indicated that MIAA and VMA combined give a predictive accuracy of 0.89 (area under the curve (AUC)); 95% confidence interval (CI) 0.78-0.99) for LAM relative to healthy women (**Fig. 1g**). Importantly, MIAA alone had an AUC of 0.84 (95% CI 0.73-0.95) for LAM relative to related pulmonary diseases (**Fig. 1g**). Thus, these results reveal novel LAM plasma biomarkers that may be complementary to VEGF-D determinations.

All identified metabolites are derived from the catabolism of monoamines mediated by monoamine oxidases A/B (MAO-A/B) and aldehyde dehydrogenases (ALDHs) (**Fig. 1h**) in the mitochondria, possibly increasing reactive oxygen species (ROS)[27]. Previous studies have shown that ROS levels are higher in *TSC2/Tsc2*-deficient cell models[28] and these cells have enhanced sensitivity to alterations of oxidative stress[24,29,30,31].

Increased Aldh and Mao expression, and Mao activity in a LAM cell model

The identified plasma metabolites may have originated from LAM lung lesions and/or the surrounding affected tissue. To assess a source from LAM cells, we first analyzed the expression of key genes and proteins. Our previous investigation showed frequent ALDH1 positivity in LAM lung lesions[20]. In the current study, we detected positivity of MAO-A and MAO-B in all lung lesions of seven LAM patients analyzed (**Fig. 2a**, top panels). In normal lung tissue from healthy individuals, MAOs were expressed in the alveolar endothelium and the luminal layer of the bronchioles (**Fig. 2a**, bottom panels). Co-staining with the LAM marker α-smooth muscle actin (αSMA) revealed co-localization with both MAO-A and MAO-B positivity in LAM lesions, with MAO-B being confined to pathological areas (**Fig. 2b**).

The expression of the *Aldh* and *Mao* genes and/or gene products was then evaluated in a LAM cell model and its corresponding control counterpart, i.e., *Tsc2*-deficient or *Tsc2*-wild-type and *Tp53*-deficient mouse embryonic fibroblasts (MEFs)[32]. Relative higher levels of most *Aldh* isoforms and of *Mao-A and Mao-B* were detected in *Tsc2*-deficient MEFs (**Fig. 2c**). Western blot assays confirmed the increase in protein expression of Aldh2 and Mao isoforms, and how the levels of these enzymes were not affected by exposure to the rapalog everolimus (**Fig. 2d**).

Tsc2-deficient MEFs cells showed a slight, but consistent emergence of ALDH-positive cells as measured by ALDEFLUOR-based assays: mean *Tsc2* wild-type percentage = 0.02 ± 0.03; mean *Tsc2*-deficient percentage = 0.31 ± 0.19 (**Fig. 2e**). Interestingly, a recent study showed that circulating human LAM

cells with loss of heterozygosity of *TSC2* have relatively high ALDH activity[33]. Moreover, we identified significantly higher Mao basal activity in *Tsc2*-deficient MEFs than in their control counterparts (**Fig. 2f**). Cells exposed to 1 μM clorgyline (Mao-A inhibitor) for 48 hours showed a reduction of this activity to zero; separately, exposure to 1 μM deprenyl (Mao-B inhibitor) for the same period reduced activity by approximately 35% (**Fig. 2f**). These effects were consistent with the basal protein expression levels of Mao-A and Mao-B (**Fig. 2d**), suggesting that both isoforms are active in the *Tsc2*-deficient cells. Furthermore, consistent with Mao activities being dependent on the cofactor flavin adenine dinucleotide (FAD), the total levels of this cofactor were found to be significantly higher in *Tsc2*-deficient MEFs (**Fig. 2g**). Therefore, expression and function of Aldh and Mao appear to be greater in LAM-related cells, and such over-activation may account for the enhanced detection of monoamine-derived metabolites in the plasma of LAM patients.

Increased ROS and mitochondrial activity in a LAM cell model

Alteration of mitochondria has previously been recognized in *Tsc1/2*-deficient cells[34,35]. Although the observed differences between *Tsc2*-deficient and wild-type MEFs might be due to altered mitochondrial content, analyses of *Vdac1*, which codes for the most abundant protein in the mitochondrial outer membrane, failed to reveal expression differences between the two MEF lines (**Fig. 3a**). Nevertheless, differences in mitochondrial morphology and homeostasis may still be present[35]. Next, since greater activity of Aldh and Mao may be linked to higher levels of mitochondrial ROS, these species were measured using MitoSOX red-based assays. The *Tsc2*-deficient MEFs showed

higher positivity and intensity of ROS signal than that of the wild-type counterpart (**Fig. 3b**). The *Tsc2*-deficient cells also showed a higher mitochondrial membrane potential as measured by MitoTracker red-based assays (**Fig. 3c**). Likewise, these MEFs exhibited higher values of basal mitochondrial respiration (**Fig. 3d**).

Since the MAO enzymes specifically produce hydrogen peroxide by oxidation of monoamines, this ROS form was subsequently measured in MEF cultures. The *Tsc2*-deficient cells showed significantly higher levels of hydrogen peroxide than the wild-type counterpart (**Fig. 3e**). This compound is decomposed into water and oxygen by the action of various enzymes, of which catalase is particularly important, and this protein was found over-expressed in *Tsc2*-deficient MEFs (**Fig. 3f**). Remarkably, consistently with increased ROS, all analyzed LAM lung tissue (7/7 patients) showed positivity for acrolein, an aldehyde that is generated endogenously through oxidation reactions (**Fig. 3g**).

Coherent with increased mitochondrial activity and ROS, *Tsc2*-deficient MEFs also displayed a slight increase in the level of HIF1α protein (**Fig. 3h**). Abnormally active mTORC1 increases the level of HIF1α-dependent gene transcription and translation, and this factor promotes the expression of VEGF-D[36]. Our studies of LAM lung lesions detected frequent positivity of HIF1α and of the mesenchymal target vimentin (5/7 cases analyzed; **Fig. 3i**). A recent publication has described increased HIF1α and mitochondrial dysfunction in candidate LAM cells isolated from lung transplants[37]. Collectively, these data depict functional links between enhanced MAO activity, ROS production and LAM biology. High levels of ROS are a hallmark of many cancer types,

contributing to their development and progression by engaging survival and stem cell-like signals[38].

Histamine-mediated signaling and metabolism in LAM

MIAA is the major metabolite of histamine excreted in urine. Histamine metabolism is altered in a range of human neoplasms, including melanoma and breast cancer, and may regulate cancer progression[39]. Cell types with active histamine metabolism are commonly responsive to histamine-mediated signaling and, among histamine receptors, HRH1 and HRH2 are the most broadly expressed in human tissue and organs. HRH1 is also expressed in breast cancer with stem cell-like features and regulates its progression[40]. Analyzing the original lung-metastatic breast cancer dataset[21] revealed a significant association between *HRH1* expression and lung metastasis events (**Supplementary Fig. S1a**). In addition, analyzing data from The Cancer Genome Atlas, the expression profiles of *HRH1* and *TSC2* were found to be negatively correlated (PCC = -0.15, $P = 2x10^{-6}$) and, conversely, *HRH1* expression was found to be positively correlated with the canonical lung-metastasis signature[21] and mTOR pathway (**Supplementary Fig. S1b**). Then, *Hrh1* was detected over-expressed in *Tsc2*-deficient relative to wild-type MEFs, but its protein levels were not substantially different (**Fig. 3f**). Importantly, however, all (7/7) LAM patients analyzed showed clear positivity for HRH1 expression in their lung lesions (**Fig. 4a**).

HRH1 is a G protein-coupled receptor that can mediate downstream signaling through SRC[41]. Activation of mTOR in LAM cells causes accumulation of active Src[42]. Analysis of active Src by its phospho-Tyr 416 (pTyr416)

294 modification showed an increase in both MEF cell lines exposed to media with
295 100 μM of histamine for 30 minutes (**Fig. 4b**). Stat3 is a down-stream functional
296 mediator of Src in LAM[42]. We observed that *Tsc2*-deficient MEFs moderately
297 increase active Stat3 (as determined by pTyr705) when exposed to histamine in
298 media without histidine, which would prevent histamine synthesis; however, a
299 contrasting effect was detected in *Tsc2* wild-type MEFs (**Fig. 4c**). In parallel,
300 *HRH1* expression was also found to be positively correlated with a SRC
301 oncogenic signature in breast cancer[43] (**Supplementary Fig. S1b**). Next,
302 exposure of MEF cultures to media without histidine revealed an inhibitory effect
303 only in *Tsc2*-deficient cells (**Fig. 4d**). Subsequently, we found that these cells
304 experience a larger synergistic inhibitory effect (combination index (CI) < 1 and
305 $P < 0.05$) when loratadine —an antagonist of HRH1— is combined with mTOR
306 inhibition (**Fig. 4e**). Compatible with this synergism and observations in LAM
307 plasma, *Tsc2*-deficient MEFs exposed to rapamycin revealed an increase of
308 histamine and a trend for a decrease of MIAA (**Fig. 4f**). Together, the data
309 indicates that histamine-mediated signaling and metabolism are active in LAM,
310 which in turn are linked to enhanced ALDHs and MAOs expression and
311 function.
312
313 **Therapeutic benefit of combining mTOR and MAO inhibitors in an *in vivo***
314 **immunodeficient LAM model**
315 Having detected abnormal expression and activity of enzymes involved in
316 monoamine metabolism, we next assessed the beneficial effect of their
317 inhibition *in vivo* by measuring the growth rate of tumor xenografts originated
318 from subcutaneous engraftment of *Tsc2*-deficient Eker rat uterine leiomyoma

(ELT3) cells in nude mice. These cells over-expressed *Maob* relative to their *TSC2*-reconstituted counterparts (**Supplementary Fig. S2**). The selected compounds for the *in vivo* assays comprised a small-molecule ALDH inhibitor (named GA11[44]) and two drugs approved to treat human neurological-related disorders: clorgyline, an MAO-A inhibitor, and rasagiline, an MAO-B inhibitor.

A pilot experiment showed no significant benefit from the monotherapies; however, the combination of clorgyline or rasagiline with everolimus (1 mg/kg/day) might produce a stronger inhibitory effect than everolimus alone (**Supplementary Fig. S3**). Following on from this pilot, drug combinations with a less effective concentration of rapamycin (0.25 mg/kg/day) were also assessed *in vivo* using the same LAM cell model. Adding clorgyline or rasagiline reduced the tumor volume by an additional 30% compared with the reduction obtained with rapamycin alone (**Fig. 5a**). The supra-additive nature of the combinations was corroborated with respect to tumor weight, which was reduced up to 65% relative to the control group (**Fig. 5b**).

As expected, rapamycin treatment reduced the levels of phospho-Ser235/236 ribosomal S6 (pS6) protein, while increasing AKT and ERK signaling (**Fig. 5c**). Subsequently, we examined markers that could explain the stronger inhibitory effect of the drug combinations relative to rapamycin alone. The pS6 levels were reduced further by the combinations, particularly when employing clorgyline (**Fig. 5d**). Decreased autophagy was also indicated by a lower LC3-II/control signal ratio in the drug combinations (**Fig. 5d**), but these settings did not show any further decrease of the autophagy substrate p62 relative to rapamycin alone (**Fig. 5c**). The proportions of senescent cells tended to be higher in the drug-treated tumors than in the control set, but cleaved

caspase-3 levels were not found to be higher in any drug-treated tumor set than in the controls (**Supplementary Fig. S4**).

To analyze the mechanistic basis of the enhanced inhibition of LAM tumorigenesis promoted by mTOR-Mao drug combinations in greater depth, the transcriptomes of two tumor xenografts from each treatment group were analyzed upon completion of the *in vivo* assays. As expected, the comparison between rapamycin-treated and control tumors showed changes of immune-related processes, accompanied by the repression of metabolic- and mitochondrial-related pathways (**Supplementary Fig. S5a**). Gene sets regulated by *TSC2*-mTOR signaling[26] also showed expected changes, validating mTOR inhibition (**Supplementary Fig. S5b**). Notably, there was a significant overlap in the genes over-expressed in both combinations relative to rapamycin alone: 9-fold enrichment, hypergeometric test $P = 4x10^{-152}$ (n = 201 common genes; **Supplementary Table S2**). Both combinations induced expression of the apoptosis-related *Bnipl* gene, which was supported by quantitative assays (**Fig. 5e**). Bnipl may also mediate mitophagy[45] and, since inhibition of Mao function may alter this organelle, we subsequently examined mitochondrial homeostasis by determining the expression of Parkin and Pink1. Both proteins showed differences relative to tumors treated solely with rapamycin: increased Parkin, but decreased Pink1 levels (**Fig. 5f**). In parallel, treatment of *Tsc2*-deficient MEF cultures with Mao inhibitors showed a decrease of mitophagy, particularly with rasagiline (**Supplementary Fig. S6**).

The commonly over-expressed genes in the drug combinations relative to rapamycin alone included *Hrh1* and, notably, *Slc18a1/Vmat1*, which is a vesicular transporter for monoamines. These over-expressions were confirmed

at the protein (Hrh1; **Fig. 5f**) and gene (*Slc18a1*; **Fig. 5g**) levels. Over-expression of Hrh1 is consistent with its induction in cells exposed to histamine[46] and with the fact that Mao activity is inhibited by clorgyline and rasagiline. Moreover, similarly to HRH1, all of the LAM lung lesions tested also revealed robust expression of SLC18A1/VMAT1 (**Fig. 5h**), further confirming altered monoamine metabolism in LAM.

In addition to specific targets, the commonly over-expressed genes in the drug combinations included many whose products promote tissue development and morphogenesis (**Fig. 5i**). Literature curation identified 27% of these genes (54/201) with established roles or associated with neural differentiation (**Fig. 5i**). This set also included the prolactin receptor (*Prlr*) gene, which is a recognized marker of breast cancer differentiation and favorable prognosis in tumors initially linked to the lung-metastatic phenotype[47]. The increased expression of *Prlr* was confirmed by quantitative assays (**Fig. 5j**). Therefore, mTOR and Mao inhibitor combinations appear to be more efficient than rapamycin alone in reducing LAM tumorigenesis, and these effects may be mediated by a combination of altering autophagy, mitochondria homeostasis, monoamine metabolism, and tumor cell phenotype.

Therapeutic benefit in an immunocompetent LAM model

The function of immune modulators has proved to be an important factor in LAM biology[48,49]. Histamine is a pro-inflammatory factor and its signaling through defined receptors can influence innate and adaptive immune responses. Therefore, we decided to evaluate the potential benefit of targeting monoamine metabolism and HRH1-mediated signaling in tumors produced by syngeneic

mouse *Tsc2*-deficient 105K cells subcutaneously engrafted in C57BL/6J mice[49]. Compared with *TSC2*-reconstituted cell counterparts, this LAM model over-expressed both Mao-A and Mao-B, and the levels of these enzymes were not affected by mTOR inhibition (**Fig. 6a**).

Unlike the assays in immunodeficient mice, *in vivo* treatment of *Tsc2*-deficient 105K tumors, revealed significant inhibitory effects in monotherapy: clorgyline, loratadine and rasagiline showed significant reductions relative to control tumors, stronger inhibitory effects being observed when the first two drugs were used (**Fig. 6b**). Intriguingly, histological examination of the tumors at conclusion of the therapeutic assays indicated higher immune cell infiltration in the loratadine-treated cases than in controls and other therapeutic settings (**Fig. 6c**). To further corroborate the effect-centered Mao function, we used two short-hairpin RNA sequences (shRNAs) directed against *Maoa* expression. The 105K cells transduced with shRNAs showed a substantial reduction of tumorigenesis; tumor growth was significantly decreased relative to controls, and 6/12 (shMaoa #1) and 4/8 (shMaoa #2) assays did not develop tumors (**Fig. 6d**). In addition to the monotherapies and shRNA-based assays, combinations of clorgyline or loratadine with rapamycin (0.25 mg/kg/day) also showed significant extra reduction of tumor growth relative to those obtained with rapamycin alone (**Fig. 6e**).

Investigation of molecular alterations underlying therapeutic responses revealed lower pTyr416 Src and Hrh1 levels in the loratadine-treated tumors (**Fig. 6f**). This setting and the clorgyline-treated tumors also showed a trend for increased levels of the Src inhibitory signal pTyr530 (**Fig. 6f**). Then, all three tested monotherapies showed lower Lc3-II/control ratios relative to controls

(**Fig. 6g**). Similar to Mao inhibitor effects, treatment of *Tsc2*-deficient MEFs with loratadine also indicated a decrease of mitophagy (**Supplementary Fig. S6**). Rapamycin combinations altered histamine-mediated signaling as indicated by increased Hrh1 levels relative to rapamycin alone (**Fig. 6h**). The combination of rapamycin and loratadine also reduced the total levels of S6 (**Fig. 6h**). Similarly to ELT3 results, there was no increase of cleaved caspase-3 (**Supplementary Fig. S7**), but examination of *Prlr* expression also showed a significant increase in the drug combinations relative to rapamycin alone (**Fig. 6i**). The notable over-expression of Prlr in the loratadine-treated tumors was confirmed by immunohistochemical assays (**Fig. 6j**). Together, these data in an immunocompetent LAM model confirm the validity of combining mTOR and Mao inhibitors, as well as extending the promise of therapeutic strategies to monotherapies based on Mao inhibitors and HRH1 antagonism.

Discussion

This study identifies novel plasma biomarkers that could improve the diagnostic process and clinical monitoring of LAM patients. Current analytical technologies enable high-throughput analysis and quantitation of metabolic biomarkers from relatively small samples. MIAA can be detected in urine and saliva, which could further facilitate the application of non-invasive clinical protocols for LAM. Indeed, the results of our study indicate that MIAA measures are independent of VEGF-D.

Following on from the evidence obtained about altered monoamine metabolism, our study provides complementary and alternative therapeutic strategies to the standard of care for LAM. The novel schemes are based on drugs approved for treating other human conditions and involve monotherapy using clorgyline or loratadine, or combinatorial regimens in which these drugs are added to relatively low doses of rapamycin. Although a combination with rasagiline may also be effective, our assays produced conflicting results between the immunodeficient and immunocompetent settings. This discrepancy can be due to the different LAM cell models employed and/or the influence of the immune system. Since enhanced activity of ALDHs and MAOs may result in increased ROS, the tumor micro-environment is likely to play an important role in determining therapeutic responses[50]. LAM lung lesions can appear very heterogeneous at the cellular level and disease cells are sensitive to tumor micro-environmental factors[51]. Intriguingly, a relevant source of histamine is mast cells, which are also major constituents of LAM lung nodules[52].

Catecholamines are metabolized through the enzymatic activities of ALDHs and MAOs. Cancer stem cells are characterized by a relative over-

457 expression and activity of certain ALDH isoforms[53], a metabolic trait associated
458 with the metastatic potential of different neoplasms including breast cancer[54].
459 *MAOA* is over-expressed in the transition from breast cancer bone metastatic
460 dormancy to relapse[55] and promotes prostate cancer metastasis[56]. MAOB
461 expression is also a prognostic factor in breast cancer[57] and gliomas, where it is
462 also positively correlated with HIF1α[58]. Our current observations in LAM-related
463 cell models, tissue and plasma are therefore consistent with a pivotal role for
464 ALDHs and MAOs in neoplastic progression and, importantly, extend on the
465 concept of LAM as a stem cell-like disease[4,20].

466 The hyperactivation of mTORC1 enhances bioenergetic and biosynthetic
467 processes that, in turn, provoke a critical burden on buffering ROS.
468 Combination of rapamycin with an inhibitor of the synthesis of the antioxidant
469 glutathione, exposure to ROS inducers, or RIP1 inhibition promote cell death in
470 *Tsc2*-deficient cell models[24,29,30,31]. Following inhibition of mTORC1, autophagy
471 is engaged as a cancer cell survival mechanism, and this action constitutes the
472 basis of combination therapies for LAM using resveratrol or chloroquine[59,60,61].
473 Our study expands on these observations by describing enhanced monoamine
474 metabolism in LAM and its link to histamine-mediated signaling. The results
475 from *in vivo* assays indicate that the therapeutic benefit of monotherapies based
476 on MAO inhibitors and HRH1 antagonism may be due to alteration of
477 autophagy and SRC-mediated signaling; the latter may be more relevant with
478 regard to loratadine effects. Intriguingly, reduction of autophagy promotes Src
479 activation in LAM cells, and this observation is the basis of an ongoing phase II
480 clinical trial (NCT02737202) testing a SRC inhibitor, saracatinib[42]. This
481 connection suggests the need for additional clinical studies to evaluate the

potential benefit of anti-histamine drugs in LAM, in monotherapy and combined with rapamycin or saracatinib.

Regarding the observed benefit of the depicted rapamycin-drug combinations, our results also suggest that alteration of autophagy, in addition to mitochondrial homeostasis and monoamine metabolism, are important underlying factors. Moreover, the novel therapeutic opportunities alter LAM tumor cell phenotype towards a relatively more differentiated state. Therefore, the corresponding approved drugs are promising alternatives for patients who do not tolerate rapamycin or who suffer continuous lung function decay with this drug.

Methods

Gene expression analyses. Metastatic breast cancer data were taken from the corresponding publication[21] and Gene Expression Omnibus (GEO) reference GSE5327. Official gene names and Entrez IDs were cross-referenced to UniProt enzymatic protein identifiers (human only and manually curated). Associated metabolites from a genome-scale metabolic network model (Recon 2.2[62]) were mapped to enzymes, resulting in a total of 47 metabolites, which were evaluated for over-represented pathways using the MetaboAnalyst[63] tool with standard parameters. Normalized breast cancer RNAseq data from the The Cancer Genome Atlas were obtained from cBioPortal and the GSEA[64] method was applied with standard parameters. The mRNAs from ELT3-V3 tumors were extracted using TRIzol (Thermo Fisher) and, following quality controls, single-end sequenced at the IRB's facility in Barcelona. The RNA-Seq reads were trimmed for adaptors, masked for low-complexity and low-quality sequences, and subsequently quantified for transcript expression using Kallisto v0.43.1[65] and rat genome build rn6. Gene-level quantification of estimated counts were obtained using tximport, rn6 and Ensembl v94 annotations. Differential expression analyses were performed using DESeq2 v2.13. GO term enrichment was analyzed using clusterProfiler[66] and GOnet[67]. The data have been deposited under GEO reference GSE129399. Literature curation was performed using the PubMed MeSH terms "neuron" or "neural" and "differentiation", in addition to each gene name; information was also extracted from the GeneCards and NCBI databases. For quantitative expression analyses, total RNA was isolated from cells or tissues using TRIzol reagent (Thermo Fisher) and complementary DNA (cDNA) synthesized using the High

Capacity cDNA Reverse Transcription Kit (Thermo Fisher) following the manufacturer's protocol. Gene expression values were measured using reverse transcription polymerase chain reactions with SYBR Green (Applied Biosystems). Control gene was *Actb* (mouse and rat) and differences were computed using the ΔΔCt method. The primer sequences used in these assays are listed in **Supplementary Table S3**.

Human samples and LAM patients. LAM patients were recruited and lung tissue samples collected by participating centers and with the support of the Spanish LAM Association (AELAM). All patients provided written informed consent and the study was approved by the ethics committees of the Bellvitge Institute for Biomedical Research (IDIBELL) and the Instituto de Investigación Sanitaria La Princesa, Hospital de Henares, Spain. VEGF-D levels were determined using the Quantikine VEGFD ELISA DVED00 kit (R&D Systems). Seven patients were not being treated with rapamycin; four used progesterone and two used bronchodilators, with two of them using both therapies. Control samples corresponded to healthy women with a similar age distribution to that of the LAM patients. LAM patient and control blood samples were collected by the same laboratory team and samples processed following a standard centrifugation protocol for plasma separation. Emphysema-related plasma samples corresponded to patients attending to the Interstitial Lung Disease Unit, Service of Pneumology, University Hospital of Bellvitge, IDIBELL, and plasma samples for patients with LAM-related pulmonary diseases were collected by the ILD Center of Excellence, St. Antonius Hospital Biobank, Nieuwegein, The Netherlands. The study was approved by the St. Antonius

Hospital ethics committee with reference R05-08A and all participants provided written informed consent.

LC-MS/MS analyses. Plasma samples (50 μl each) were mixed with 300 μl cold methanol:water, vortexed and cold centrifuged. Cell pellets were scrapped, collected and frozen. The pellets were resuspended in cold methanol:water and metabolite lysates purified with three rounds of liquid N_2 immersion and sonication, followed by 1 hour in ice before centrifugation. For the cell culture assays, 100 μl of media were lyophilized and resuspended in cold methanol:water. The extracts were analyzed by an ultra-high performance LC system coupled to a 6490 triple-quadrupole mass spectrometer (QqQ, Agilent Technologies) with electrospray ion source (LC-ESI-QqQ) working in positive mode. Two μl of plasma extract and 1 μl of cell and media extract were injected to the LC system. An ACQUITY UPLC HSS T3 column (1.8 μm, 2.1×150 mm, Waters) and a gradient mobile phase consisting of water with 0.1% formic acid (phase A) and acetonitrile with 0.1% formic acid (phase B) were used for chromatographic separation. The gradient was as follows: isocratic for 2 minutes at 10% B, from 2 to 3 minutes raised to 80% B, 80% B was maintained for 30 seconds, until 4 minutes the percentage of B decreased to 10% and finally column equilibrated at 10% B until 7 minutes. The flow of the method was 0.3 ml/min. The mass spectrometer parameters were as follows: drying and sheath gas temperatures 120ºC and 400ºC, respectively; source and sheath gas flows 19 and 12 l/min, respectively; nebulizer flow 20 psi; capillary voltage 2100 V; nozzle voltage 500 V; and iFunnel HRF and LRF 150 and 60 V, respectively. The QqQ worked in MRM mode using defined transitions.

Immunohistochemistry and immunohistofluorescence. The assays were performed on serial paraffin sections using the EnVision kit (Dako). Antigen were retrieved using citrate-based (pH 6) or EDTA-based (pH 9) buffers. Endogenous peroxidase was blocked by pre-incubation in a solution of 3% H_2O_2 performed in 1x phosphate-buffered saline with 10% goat serum. Slides were incubated overnight at 4ºC with primary antibody diluted in blocking solution. Secondary anti-mouse or anti-rabbit peroxidase-conjugated antibodies (Envision+ system-HRP, Dako) were used. Sections were hematoxylin-counterstained and examined with a Nikon Eclipse 80i microscope. Quantifications were performed using ImageJ software. For immunohistofluorescence, the slides were incubated with a mix of the two primary antibodies (anti-α-SMA and anti-MAO-A/B). In this case, the secondary antibodies used were goat anti-mouse Alexa-488 and goat anti-rabbit Alexa-546 (Thermo Fisher). Sudan black staining was performed to avoid paraffin auto-fluorescence. The sections were counterstained with DAPI, mounted with coverslips in Fluoromount® Aqueous Mounting Medium (Sigma), and visualized in a Fluorescence DM6000 microscope (Leica Microsystems).

Cell lines and media. This study used MEFs derived from *Tsc2/Tp53* or *Tp53* knockout mice; *Tsc2*-mutant and *TSC2*-reconstituted Eker rat uterine leiomyoma cells (ELT3-V3 and ELT3-T3, respectively); and *Tsc2*-deficient and *TSC2*-reconstituted mouse kidney cystadenoma cells (105K) cells. The cell cultures were based on Dulbecco's modified Eagle's (DMEM) media supplemented with 10% fetal bovine serum (Gibco), except for ELT3 cells, for which DMEM-F12 supplemented with 10% or 0.5% FBS (as indicated) was used. Media without histidine was purchased from US Biological (D9801-02).

Cell-based assays. MAO activity was monitored using a radiometric assay with ^{14}C-tyramine hydrochloride as substrate. Data were normalized for protein content and rates expressed as disintegrations of 14C/min/μg protein. ALDH activity was determined using an ALDEFLUOR assay kit (STEMCELL Technologies) following the manufacturer's protocol, and analyzed with a Gallios flow cytometer (Beckman Coulter). The intracellular production of FAD was measured using the FAD Colorimetric Assay Kit (BioVision) following the manufacturer's protocol. Samples were homogenized and deproteinized using perchloric acid precipitation. Samples and standards were then incubated with the FAD enzyme mix, OxiRed Probe, and assay buffer for 15-60 minutes in triplicate, and measured by the colorimetric method (λ = 570 nm). MitoSOX Red (Thermo Fisher) was used to quantify mitochondrial superoxide production. Cells seeded in 6-well plates were incubated with 5 μM of MitoSOX dye diluted in Hank's Buffered Salt Solution (HBSS) for 10 minutes at 37ºC. Staining was then measured by flow cytometry. The MitoTracker Red CMXRos (Thermo Fisher) was used to measure mitochondrial membrane potential. Cells seeded in 6-well plates were incubated with 500 nM MitoTracker dye diluted in PBS for 30 minutes at 37ºC, and the staining was analyzed by flow cytometry. Assays were performed in duplicate for each condition. The high-resolution Oxygraph-2K (Oroboros Instruments) was used to measure the oxygen consumption in cells. In brief, a concentration of 10^6 cells/ml diluted in medium was placed in the closed respirometer chamber to measure basal oxygen consumption. Oxygen flux was recorded constantly using DatLab software 4.3 (Oroboros Instruments) and the values obtained were directly proportional to the oxygen consumption. To analyze viability, cells were plated into 96-well plates (500-

2500 per well) in triplicate and treated for 72 hours. Cell viability was evaluated with 2,3-bis-(2-methoxy-4-nitro-5-sulfophenyl)-2H-tetrazolium-5-carboxanilide (XTT, Sigma-Aldrich). The results were evaluated relative to control solution-treated cells. The Chou-Talalay[68] method in ComboSyn was used to identify synergistic drug combinations. For mitophagy assays, 50,000 MEFs of each condition and stably expressing the pH-sensitive mt-Keima reporter plasmid were analyzed by flow cytometry as described previously[69].

Compounds and antibodies. Clorgyline was purchased from Sigma-Aldrich and everolimus, loratadine, rapamycin, and rasagiline were purchased from Selleck Chemicals. GA11 was synthesized in the Department of Pharmacy, University of Pisa, Italy. The antibodies used in this study were: anti-acrolein (ab48501, Abcam), anti-actin (SC-8432, Santa Cruz Biotechnology), anti-total and pSer473 Akt (9272 and 4051, respectively; Cell Signaling Technology), anti-Aldh2 (SC-166362, Santa Cruz Biotechnology), anti-Cat (ab52477, Abcam), anti-total and pThr202/Tyr204 Erk (9102 and 9101, respectively, Cell Signaling Technology), anti-β-galactosidase (orb100205, Biorbyt), anti-Hif1α (NB100-105SS, Novus Biologicals), anti-Hrh1 (PA5-27817, Thermo Fisher), anti-Lc3 (PM036, MBL International), anti-Mao/MAO-A (ab126751, Abcam), anti-Mao/MAO-B (HPA002328, Thermo Fisher), anti-p62 (5114, Cell Signaling Technology), anti-Parkin (P6248, Sigma-Aldrich), anti-Pink1 (ab23707, Abcam), anti-Prlr (SC-30225, Santa Cruz Biotechnology), anti-total and pS6 (SC-74459, Santa Cruz Biotechnology; and 2211, Cell Signaling Technology), anti-αSMA (A2547, Sigma-Aldrich), anti-total, pTyr416 and pTyr530 Src (2108, 2101 and 2105, respectively, Cell Signaling Technology), anti-total and pTyr705 Stat3 (9139 and 9134, respectively, Cell Signaling Technology), anti-tubulin

(ab44928, Abcam), anti-Vdac1 (ab15895, Abcam), anti-vimentin (SC-6260, Santa Cruz Biotechnology), anti-vinculin (V9131, Sigma-Aldrich), and anti-Vmat1 (SC-166391, Santa Cruz Biotechnology).

Western blot assays. Cells or tissues were lysed in radioimmunoprecipitation assay (RIPA) buffer supplemented with protease inhibitor (cOmplete, Sigma-Aldrich) and phosphatase inhibitor (PhosSTOP, Sigma-Aldrich) cocktails. Protein concentrations were measured using the Thermo Scientific Pierce BCA Protein assay. Lysates were resolved in sodium dodecyl sulfate-polyacrylamide electrophoresis gels and transferred to polyvinylidene difluoride (PVDF) membranes (Sigma-Aldrich). Target proteins were detected using antibodies listed above and chemiluminescence with the Nove ECL Chemiluminescent Substrate Reagent Kit (Thermo Fisher) in the ChemiDoc™ Imaging System (Bio-Rad).

***In vivo* experiments.** The IDIBELL's Animal Care and Use Committee approved the animal studies. Six-week-old female NOD-scid mice were purchased from Charles River, inoculated subcutaneously with ELT3-V3 cells (2×10^6 cells per injection/site/mouse). When tumors reached a volume of 150-200 mm^3 they were randomly assigned to control and treatment groups. The drugs were administrated as follows: vehicle control (0.2% carboxymethylcellulose (CMC) and 0.25% Tween-80; intraperitoneal), everolimus or rapamycin (1 or 0.25 mg/kg/day in CMC; intraperitoneal), GA11 (20 mg/kg/day in CMC; intraperitoneal), clorgyline (10 mg/kg/day in phosphate-buffered saline (PBS); intraperitoneal), and rasagiline (1 mg/kg/day in PBS; intraperitoneal). Six-week-old female C57BL/6J mice were purchased from Charles River, inoculated with 105K cells (2.5×10^6 cells) in Matrigel (Corning).

When tumors attained a volume of 50-100 mm^3 (monotherapy) or 150-200 mm^3 (rapamycin and its combinations) they were randomly assigned to control and treatment groups. The drugs were administered as detailed above and/or with loratadine (25 mg/kg/day in CMC; intraperitoneal). For shMAOA assays, the following MISSION (Sigma-Aldrich) constructs were used: TRCN0000327502 and TRCN0000327503. The 105K cells (2.5 million) were injected subcutaneously and tumor growth measured weekly starting at a volume of approximately 50 mm^3.

Statistical analyses. The significance of the difference of metabolite values between two given plasma sets was determined from a two-tailed Mann-Whitney test. The comparison of paired values was based on the Wilcoxon signed-rank test. Model selection was determined by stepwise regression with the AIC criterion using the stepAIC function in R software. Differences in levels of gene and protein expression among cell lines or tumor assays were assessed using the *t*-test if data normality was fulfilled, otherwise the Mann-Whitney test was applied. Tumor growth values on each day of treatment were examined to determine if they were normally distributed and, if so, one-tailed *t*-tests were applied for comparisons to a reference group; otherwise, Mann-Whitney tests were applied.

Acknowledgments

This work is dedicated to the memory of Dr. Antoni Xaubet, who contributed to the initiation of LAM studies. We wish to thank the individuals who provided blood samples for their contribution, and the AELAM foundation for its continuous support of LAM research. We also thank Prof. E. Henske for

691 providing the LAM cell models. The metabolic studies were performed thanks to
692 the technological infrastructure of the Centre for Omic Sciences (COS),
693 Nutrition and Health Technology Centre (CTNS), Reus, Spain. This research
694 was supported by AELAM, Carlos III Institute of Health grants PI15/00854 and
695 PI18/01029 (co-funded by European Regional Development Fund (ERDF), a
696 way to build Europe), Generalitat de Catalunya SGR grants 2014-364 and
697 2017-449, and CERCA Program, and ZonMW-TopZorg grant 842002003.
698 C.L.M. acknowledges the financial support (PRA-2017-51 project) of the
699 University of Pisa. A.U.K. is supported by Nottingham Trent University
700 Independent Fellowship Scheme. The results here are in part based upon data
701 generated by the TCGA Research Network (https://www.cancer.gov/tcga) and
702 we would like to express our thankfulness to the TCGA consortia and
703 coordinators for data production and clinical information used in this study.
704

Competing interests

M.A.P. is recipient of an unrestricted research grant from Roche Pharma for the development of the ProCURE ICO research program.

Author contributions

M.A.P. designed the study and wrote the paper; C.H., F.M. and N.G performed experiments in vivo; C.H., F.M., N.G, A.I.E., J.M.C., R.G., C.B., C.G. and M.A.P. analyzed data of in vivo experiments; C.H., F.M., G.R.G. and A.B. performed experiments in vitro; C.H., F.M., G.R.G., A.B., J.A.M., J.C.P., F.V., A.A., X.Z., R.H., M.F. and M.A.P. analyzed data of in vitro experiments; A.J., J.C. and O.Y performed metabolite analyses; A.G., L.P., R.E. and M.A.P. performed bioinformatic analyses; C.H., F.M., A.G., L.P. and M.A.P. provided statistical analysis; S.R.J. and S.M. performed VEGF-D determinations; A.C., E.R-.L., M.M-.M., A.M., C.M., E.L., J.A.R-.P., C.V., T.A., P.U., R.L., A.X., J.A., C.H.M.M., J.J.V., M.J.R.Q. and A.R. collected patient samples and clinical data; C.L.M. produced GA11; A.N-.C. and M.M. provided histamine receptors data; H.F. performed mitophagy assays; C.H., A.U-.K. and E.B. performed Mao activity assays.

Data availability

RNA sequencing data have been deposited under the Gene Expression Omnibus reference GSE129399.

Reviewer access token: ktihcqwadjarvmh

References

1. Johnson, S. R., Taveira-DaSilva, A. M. & Moss, J. Lymphangioleiomyomatosis. *Clin. Chest Med.* **37**, 389–403 (2016).
2. Krymskaya, V. P. & McCormack, F. X. Lymphangioleiomyomatosis: a monogenic model of malignancy. *Annu. Rev. Med.* **68**, 69–83 (2017).
3. Yu, J. & Henske, E. P. mTOR activation, lymphangiogenesis, and estrogen-mediated cell survival: the 'perfect storm' of pro-metastatic factors in LAM pathogenesis. *Lymphat Res Biol* **8**, 43–49 (2010).
4. Henske, E. P. & McCormack, F. X. Lymphangioleiomyomatosis - a wolf in sheep's clothing. *J. Clin. Invest.* **122**, 3807–3816 (2012).
5. Carsillo, T., Astrinidis, A. & Henske, E. P. Mutations in the tuberous sclerosis complex gene *TSC2* are a cause of sporadic pulmonary lymphangioleiomyomatosis. *Proc. Natl. Acad. Sci. U.S.A.* **97**, 6085–6090 (2000).
6. Astrinidis, A. *et al.* Mutational analysis of the tuberous sclerosis gene *TSC2* in patients with pulmonary lymphangioleiomyomatosis. *J. Med. Genet.* **37**, 55–57 (2000).
7. Muzykewicz, D. A. *et al. TSC1* and *TSC2* mutations in patients with lymphangioleiomyomatosis and tuberous sclerosis complex. *J. Med. Genet.* **46**, 465–468 (2009).
8. Crino, P. B., Nathanson, K. L. & Henske, E. P. The tuberous sclerosis complex. *N. Engl. J. Med.* **355**, 1345–1356 (2006).
9. Saxton, R. A. & Sabatini, D. M. mTOR signaling in growth, metabolism, and disease. *Cell* **169**, 361–371 (2017).
10. Johnson, S. R. *et al.* European Respiratory Society guidelines for the diagnosis and management of lymphangioleiomyomatosis. *Eur. Respir. J.* **35**, 14–26 (2010).
11. McCormack, F. X. *et al.* Official American Thoracic Society/Japanese Respiratory Society Clinical Practice guidelines: lymphangioleiomyomatosis diagnosis and management. *Am. J. Respir. Crit. Care Med.* **194**, 748–761 (2016).
12. McCormack, F. X. *et al.* Efficacy and safety of sirolimus in lymphangioleiomyomatosis. *N. Engl. J. Med.* **364**, 1595–1606 (2011).
13. Young, L. *et al.* Serum VEGF-D a concentration as a biomarker of lymphangioleiomyomatosis severity and treatment response: a prospective analysis of the Multicenter International Lymphangioleiomyomatosis Efficacy of Sirolimus (MILES) trial. *Lancet Respir Med* **1**, 445–452 (2013).
14. Taveira-DaSilva, A. M., Jones, A. M., Julien-Williams, P., Stylianou, M. & Moss, J. Long-term effect of sirolimus on serum vascular endothelial growth factor D levels in patients with lymphangioleiomyomatosis. *Chest* **153**, 124–132 (2018).
15. Bissler, J. J. *et al.* Sirolimus for angiomyolipoma in tuberous sclerosis complex or lymphangioleiomyomatosis. *N. Engl. J. Med.* **358**, 140–151 (2008).
16. Bee, J., Bhatt, R., McCafferty, I. & Johnson, S. R. A 4-year prospective evaluation of protocols to improve clinical outcomes for patients with lymphangioleiomyomatosis in a national clinical centre. *Thorax* **70**, 1202–1204 (2015).
17. Yao, J. *et al.* Sustained effects of sirolimus on lung function and cystic lung

lesions in lymphangioleiomyomatosis. *Am. J. Respir. Crit. Care Med.* **190**, 1273–1282 (2014).
18. Bee, J., Fuller, S., Miller, S. & Johnson, S. R. Lung function response and side effects to rapamycin for lymphangioleiomyomatosis: a prospective national cohort study. *Thorax* **73**, 369–375 (2018).
19. Mateo, F. *et al.* Stem cell-like transcriptional reprogramming mediates metastatic resistance to mTOR inhibition. *Oncogene* **36**, 2737–2749 (2017).
20. Ruiz de Garibay, G. *et al.* Lymphangioleiomyomatosis biomarkers linked to lung metastatic potential and cell stemness. *PLoS One* **10**, e0132546 (2015).
21. Minn, A. J. *et al.* Genes that mediate breast cancer metastasis to lung. *Nature* **436**, 518–524 (2005).
22. Jiang, W. G. *et al.* Tuberin and hamartin are aberrantly expressed and linked to clinical outcome in human breast cancer: the role of promoter methylation of *TSC* genes. *Eur. J. Cancer* **41**, 1628–1636 (2005).
23. Sun, Y. *et al.* Estradiol promotes pentose phosphate pathway addiction and cell survival via reactivation of Akt in mTORC1 hyperactive cells. *Cell Death Dis* **5**, e1231 (2014).
24. Li, J. *et al.* mTORC1-driven tumor cells are highly sensitive to therapeutic targeting by antagonists of oxidative stress. *Cancer Res.* **76**, 4816–4827 (2016).
25. Yecies, J. L. & Manning, B. D. Transcriptional control of cellular metabolism by mTOR signaling. *Cancer Res.* **71**, 2815–2820 (2011).
26. Düvel, K. *et al.* Activation of a metabolic gene regulatory network downstream of mTOR complex 1. *Mol. Cell* **39**, 171–183 (2010).
27. Ugun-Klusek, A. *et al.* Monoamine oxidase-A promotes protective autophagy in human SH-SY5Y neuroblastoma cells through Bcl-2 phosphorylation. *Redox Biol* **20**, 167–181 (2019).
28. Finlay, G. A., Thannickal, V. J., Fanburg, B. L. & Kwiatkowski, D. J. Platelet-derived growth factor-induced p42/44 mitogen-activated protein kinase activation and cellular growth is mediated by reactive oxygen species in the absence of TSC2/tuberin. *Cancer Res.* **65**, 10881–10890 (2005).
29. Medvetz, D. *et al.* High-throughput drug screen identifies chelerythrine as a selective inducer of death in a TSC2-null setting. *Mol. Cancer Res.* **13**, 50–62 (2015).
30. Filipczak, P. T. *et al.* TSC2 deficiency unmasks a novel necrosis pathway that is suppressed by the RIP1/RIP3/MLKL signaling cascade. *Cancer Res.* **76**, 7130–7139 (2016).
31. Lam, H. C. *et al.* p62/SQSTM1 cooperates with hyperactive mTORC1 to regulate glutathione production, maintain mitochondrial integrity, and promote tumorigenesis. *Cancer Res.* **77**, 3255–3267 (2017).
32. Zhang, H. *et al.* Loss of Tsc1/Tsc2 activates mTOR and disrupts PI3K-Akt signaling through downregulation of PDGFR. *J. Clin. Invest.* **112**, 1223–1233 (2003).
33. Pacheco-Rodríguez, G. *et al.* Circulating lymphangioleiomyomatosis tumor cells with loss of heterozygosity in the *TSC2* gene show increased aldehyde dehydrogenase activity. *Chest* S0012-3692(19)30874-8 (2019).
34. Goto, J. *et al.* Regulable neural progenitor-specific Tsc1 loss yields giant cells with organellar dysfunction in a model of tuberous sclerosis complex. *Proc. Natl. Acad. Sci. U.S.A.* **108**, E1070-1079 (2011).

35. Ebrahimi-Fakhari, D. *et al.* Impaired mitochondrial dynamics and mitophagy in neuronal models of tuberous sclerosis complex. *Cell Rep* **17**, 1053–1070 (2016).
36. Brugarolas, J. B., Vazquez, F., Reddy, A., Sellers, W. R. & Kaelin, W. G. TSC2 regulates VEGF through mTOR-dependent and -independent pathways. *Cancer Cell* **4**, 147–158 (2003).
37. Abdelwahab, E. M. M. *et al.* Mitochondrial dysfunction is a key determinant of the rare disease lymphangioleiomyomatosis and provides a novel therapeutic target. *Oncogene* **38**, 3093–3101 (2018).
38. Hanahan, D. & Weinberg, R. A. Hallmarks of cancer: the next generation. *Cell* **144**, 646–674 (2011).
39. Medina, V. *et al.* Histamine-mediated signaling processes in human malignant mammary cells. *Cancer Biol. Ther.* **5**, 1462–1471 (2006).
40. Fernández-Nogueira, P. *et al.* Histamine receptor 1 inhibition enhances antitumor therapeutic responses through extracellular signal-regulated kinase (ERK) activation in breast cancer. *Cancer Lett.* **424**, 70–83 (2018).
41. Luttrell, D. K. & Luttrell, L. M. Not so strange bedfellows: G-protein-coupled receptors and Src family kinases. *Oncogene* **23**, 7969–7978 (2004).
42. Tyryshkin, A., Bhattacharya, A. & Eissa, N. T. SRC kinase is a novel therapeutic target in lymphangioleiomyomatosis. *Cancer Res.* **74**, 1996–2005 (2014).
43. Bild, A. H. *et al.* Oncogenic pathway signatures in human cancers as a guide to targeted therapies. *Nature* **439**, 353–357 (2006).
44. Cheng, P. *et al.* FOXD1-ALDH1A3 signaling is a determinant for the self-renewal and tumorigenicity of mesenchymal glioma stem cells. *Cancer Res.* **76**, 7219–7230 (2016).
45. O'Sullivan, T. E., Johnson, L. R., Kang, H. H. & Sun, J. C. BNIP3- and BNIP3L-mediated mitophagy promotes the generation of natural killer cell memory. *Immunity* **43**, 331–342 (2015).
46. Das, A. K. *et al.* Stimulation of histamine H1 receptor up-regulates histamine H1 receptor itself through activation of receptor gene transcription. *J. Pharmacol. Sci.* **103**, 374–382 (2007).
47. López-Ozuna, V. M., Hachim, I. Y., Hachim, M. Y., Lebrun, J.-J. & Ali, S. Prolactin pro-differentiation pathway in triple negative breast cancer: impact on prognosis and potential therapy. *Sci Rep* **6**, 30934 (2016).
48. Maisel, K. *et al.* Immune checkpoint ligand PD-L1 is upregulated in pulmonary lymphangioleiomyomatosis. *Am. J. Respir. Cell Mol. Biol.* **59**, 723–732 (2018).
49. Liu, H.-J. *et al.* TSC2-deficient tumors have evidence of T cell exhaustion and respond to anti-PD-1/anti-CTLA-4 immunotherapy. *JCI Insight* **3**, e98674 (2018).
50. Gorrini, C., Harris, I. S. & Mak, T. W. Modulation of oxidative stress as an anticancer strategy. *Nat Rev Drug Discov* **12**, 931–947 (2013).
51. Pacheco-Rodriguez, G. & Moss, J. The role of chemokines in migration of metastatic-like lymphangioleiomyomatosis cells. *Crit. Rev. Immunol.* **30**, 387–394 (2010).
52. Valencia, J. C. *et al.* Tissue-specific renin-angiotensin system in pulmonary lymphangioleiomyomatosis. *Am. J. Respir. Cell Mol. Biol.* **35**, 40–47 (2006).
53. Toledo-Guzmán, M. E., Ibañez Hernández, M., Gomez-Gallegos, A. A. & Ortiz-Sánchez, E. ALDH as a stem cell marker in solid tumors. *Curr Stem*

878 *Cell Res Ther* (2018). doi:10.2174/1574888X13666180810120012
879 54. Ginestier, C. *et al.* ALDH1 is a marker of normal and malignant human
880 mammary stem cells and a predictor of poor clinical outcome. *Cell Stem*
881 *Cell* **1**, 555–567 (2007).
882 55. Lu, X. *et al.* VCAM-1 promotes osteolytic expansion of indolent bone
883 micrometastasis of breast cancer by engaging α4β1-positive osteoclast
884 progenitors. *Cancer Cell* **20**, 701–714 (2011).
885 56. Wu, J. B. *et al.* MAOA-dependent activation of Shh-IL6-RANKL signaling
886 network promotes prostate cancer metastasis by engaging tumor-stromal
887 cell interactions. *Cancer Cell* **31**, 368–382 (2017).
888 57. Cha, Y. J., Jung, W. H. & Koo, J. S. Site-specific expression of amine
889 oxidases in breast cancer metastases. *Tumour Biol.* **40**,
890 1010428318776822 (2018).
891 58. Sharpe, M. A. & Baskin, D. S. Monoamine oxidase B levels are highly
892 expressed in human gliomas and are correlated with the expression of HiF-
893 1α and with transcription factors Sp1 and Sp3. *Oncotarget* **7**, 3379–3393
894 (2016).
895 59. Parkhitko, A. *et al.* Tumorigenesis in tuberous sclerosis complex is
896 autophagy and p62/sequestosome 1 (SQSTM1)-dependent. *Proc. Natl.*
897 *Acad. Sci. U.S.A.* **108**, 12455–12460 (2011).
898 60. Alayev, A. *et al.* Effects of combining rapamycin and resveratrol on
899 apoptosis and growth of TSC2-deficient xenograft tumors. *Am. J. Respir.*
900 *Cell Mol. Biol.* **53**, 637–646 (2015).
901 61. El-Chemaly, S. *et al.* Sirolimus and autophagy inhibition in
902 lymphangioleiomyomatosis: results of a phase I clinical trial. *Chest* **151**,
903 1302–1310 (2017).
904 62. Swainston, N. *et al.* Recon 2.2: from reconstruction to model of human
905 metabolism. *Metabolomics* **12**, 109 (2016).
906 63. Chong, J. *et al.* MetaboAnalyst 4.0: towards more transparent and
907 integrative metabolomics analysis. *Nucleic Acids Res.* **46**, W486–W494
908 (2018).
909 64. Subramanian, A. *et al.* Gene set enrichment analysis: a knowledge-based
910 approach for interpreting genome-wide expression profiles. *Proc. Natl.*
911 *Acad. Sci. U.S.A.* **102**, 15545–15550 (2005).
912 65. Bray, N. L., Pimentel, H., Melsted, P. & Pachter, L. Near-optimal
913 probabilistic RNA-seq quantification. *Nat. Biotechnol.* **34**, 525–527 (2016).
914 66. Yu, G., Wang, L.-G., Han, Y. & He, Q.-Y. clusterProfiler: an R package for
915 comparing biological themes among gene clusters. *OMICS* **16**, 284–287
916 (2012).
917 67. Pomaznoy, M., Ha, B. & Peters, B. GOnet: a tool for interactive Gene
918 Ontology analysis. *BMC Bioinformatics* **19**, 470 (2018).
919 68. Chou, T.-C. Drug combination studies and their synergy quantification using
920 the Chou-Talalay method. *Cancer Res.* **70**, 440–446 (2010).
921 69. Um, J.-H., Kim, Y. Y., Finkel, T. & Yun, J. Sensitive measurement of
922 mitophagy by flow cytometry using the pH-dependent fluorescent reporter
923 mt-Keima. *J Vis Exp* (2018). doi:10.3791/58099
924

925

FIGURE LEGENDS

Fig. 1. Identification of novel LAM plasma biomarkers. a Strategy for identifying metabolic plasma biomarkers and, subsequently, therapeutic opportunities for LAM based on the analysis of lung-metastatic breast cancer gene expression data. **b** Significantly enriched metabolic pathways among the 30 enzymes identified in the previous analysis. **c** Plasma MIAA levels for indicated settings. The asterisks correspond to significant differences: *P < 0.05, **P < 0.01, ***P < 0.001, and ****P < 0.0001. Bars indicate means and standard deviations (SDs). **d** Lack of correlation between MIAA and VEGF-D levels (n.s., not significant). **e** Higher plasma MIAA levels in LAM patients with no therapy or other therapies relative to rapamycin-treated. **f** Plasma levels of three other metabolic products derived from monoamine metabolism and showing significant differences with controls and/or between LAM and related pulmonary diseases. **g** Receiver operating characteristic (ROC) curves and the corresponding AUC and Akaike information criterion (AIC) values for the analyzed metabolites comparing LAM and healthy (top) or related pulmonary disease (bottom) plasma results. **h** Representation of enzymatic reactions giving rise to the identified metabolites.

Fig. 2. Expression and function of ALDHs/Aldhs and/or MAOs/Maos in LAM tissue and cell model. a Representative images of immunohistochemical positivity of MAO-A/B in LAM lung lesions (top panels, two patients) and healthy lung (bottom panels). Brown-stained cells define positivity, counter stained with hematoxylin. Scale bars are shown. **b** Representative images of immunofluorescence detection of MAO-A/B and α-SMA in LAM lung lesions,

co-stained with 4',6-diamidino-2-phenylindole (DAPI, merged). **c** Graph showing gene expression differences (log-fold changes) of defined genes (X-axis) in *Tsc2*-deficient relative to wild-type MEFs. The asterisks indicate significant differences (Mann-Whitney test *P* values). The bars indicate means and SDs. Dotted horizontal lines indicate 2-fold (top) and 0.5-fold (bottom) changes. **d** Western blot of key proteins detected in *Tsc2*-deficient and wild-type MEFs in DMSO-exposed conditions or treated with 20 nM everolimus for 16 hours. Loading controls (tubulin and actin) are shown. pS6: phospho-Ser235/Ser236 ribosomal protein S6. **e** Representative flow cytometry results showing cell percentages for ALDEFLUOR-positive cells. **f** Quantified Mao basal activity (Y-axis) in MEF cell culture conditions as depicted on the X-axis and in the inset. The significant differences are indicated. CPM: counts per minute. **g** Quantified FAD in MEF cell cultures as depicted in the inset. The significant difference is indicated.

Fig. 3. Mitochondrial activity and ROS in the LAM cell model, and potential consequences on LAM lesions. a Expression of *Vdac1*/Vdac1 in MEF cell lines, as indicated. **b** Representative flow cytometry results (total n = 3) showing a higher percentage of MitoSox red-positive cells in *Tsc2*-deficient MEFs. **c** Representative flow cytometry results (n = 3) showing a higher intensity (X-axis) of MitoTracker red-positive cells in *Tsc2*-deficient MEFs. **d** Higher basal mitochondrial respiration (as measured by oxygen consumption, Y-axis; n = 2) in *Tsc2*-deficient MEFs. **e** Graph showing higher hydroxide peroxide levels in *Tsc2*-deficient MEF cultures across different numbers of cells analyzed (X-axis; n = 2). **f** Left panel, western blot results showing relative over-expression of

976 catalase (Cat) in *Tsc2*-deficient MEFs, and unaffected by exposure to
977 everolimus. Right panel, graph showing gene expression differences (log-fold
978 changes) of *Cat* and *Hrh1* (subsequent sections) in *Tsc2*-deficient relative to
979 wild-type MEFs. The asterisks indicate significant differences (Mann-Whitney
980 test *P* values). **g** Representative images of immunohistochemical detection of
981 acrolein in LAM lung lesions (two patients). **h** Western blot showing relatively
982 higher expression of Hif1α in *Tsc2*-deficient MEF cell extracts, and increase
983 with exposure to everolimus. **i** Representative images of immunohistochemical
984 detection of HIF1α and VIM in LAM lung lesions (two patients).
985
986 **Fig. 4. Histamine-mediated signaling in LAM. a** Representative images of
987 immunohistochemical detection of H□□□ in LAM lung lesions (two patients). **b**
988 Western blot results showing a relative increase of pTyr416 Src signal in both
989 MEF cell lines exposed to histamine (media DMEM with 0.5% fetal bovine
990 serum (FBS)). **c** Western blot results showing a relative increase of pTyr705
991 Stat3 signal in *Tsc2*-deficient MEFs and a decrease in wild-type MEFs, exposed
992 to histamine in media (DMEM 0.5% FBS) without histidine. **d** Graph showing
993 inhibition of *Tsc2*-deficient MEF viability, but not of wild-type MEFs, in media
994 without histidine (two different DMEM-based conditions are shown). **e** Cell
995 viability inhibitory effect of loratadine alone or combined (variable dose, X-axis)
996 with everolimus (20 nM) in *Tsc2*-deficient and wild-type MEF cultures. The
997 synergistic combination indexes (CIs; values < 1) are shown. **f** Box plot showing
998 fold-change peak area values (four replicates) of histamine and MIAA in
999 rapamycin-treated relative to control *Tsc2*-deficient MEFs. The significant
1000 difference is indicated.

Fig. 5. Therapeutic benefit of rapamycin in addition to clorgyline or rasagiline in an immunodeficient LAM model. a *Tsc2*-deficient ELT3 tumor growth rates under treatment conditions as indicated in the inset. Asterisks indicate significant reduction due to drug combinations (one-tailed *t*-test *P* values) relative to rapamycin alone. **b** *Tsc2*-deficient ELT3 tumor volume changes at the end of the therapeutic assays. **c** Western blot results for key markers analyzed in representative tumors from each treatment group. **d** Top and middle panels, western blot results for pS6, total S6, Lc3-I/II and loading control vinculin in tumors treated with rapamycin alone or combined with a Mao inhibitor. Bottom panel, levels of Lc3-II and pS6 relative to controls; significant differences (one-tailed Mann-Whitney test *P* values) are indicated. **e** Quantification of *Bnipl* expression in tumors of each treatment group (n = 4-5/group). The asterisk indicates significant difference (one-tailed Mann-Whitney test *P* value). **f** Top and middle panels, western blot results for Hrh1, Parkin, Pink1, and loading control tubulin in tumors treated with rapamycin alone or combined with a Mao inhibitor. Bottom panel, results of signal quantifications; significant differences (one-tailed Mann-Whitney test *P* values) are shown. **g** Graph of relative levels of *Slc18a1* in tumors of each treatment group (n = 4-5/group). The asterisk indicates significant difference (one-tailed Mann-Whitney test *P* value). **h** Representative images of immunohistochemical detection of SLC18A1/VMAT1 in LAM lung lesions (two patients). **i** Network showing significantly (false discovery rate < 5%) over-represented GO terms among over-expressed genes in the drug combinations relative to rapamycin alone, and genes associated with neuronal differentiation in the literature, as indicated

in the inset. The network edges link over-represented GO terms to genes. Single genes involved in neuronal differentiation but without an enriched term are also shown. **j** Quantification of *Prlr* expression in tumors of each treatment group (n = 4-5/group). The asterisk indicates significant difference (one-tailed Mann-Whitney test *P* value).

Fig. 6. Therapeutic benefits of clorgyline, rasagiline and loratadine in an immunocompetent LAM model. a Western blot results for key proteins including Mao-A/B in *Tsc2*-deficient and *TSC2*-reconstituted 105K cells. **b** Graph showing *Tsc2*-deficient 105K tumor growth rates under different monotherapies, as indicated in the inset. Asterisks indicate significant reductions (one-tailed *t*-test *P* values) relative to controls. **c** Top panel, graph showing quantification of immune cell infiltration in 105K tumors at completion of the therapeutic assays. The significant difference is indicated. Bottom panel, representative magnified HE images. **d** Left panel, graph showing *Tsc2*-deficient 105K tumor growth rates from cells depleted of Mao-A expression or control. Right panel, confirmation of *Maoa* expression depletion by the shRNAs. **e** Graph showing *Tsc2*-deficient 105K tumor growth rates under rapamycin and rapamycin-combined therapies, as indicated in the inset. Asterisks indicate significant reductions (one tailed *t*-test *P* values) relative to rapamycin alone. **f** Left panels, western blot results showing differences in pTyr416 and pTyr530 Src, and Hrh1 expression in certain monotherapies relative to controls. Right panels, results of signal quantifications; significant differences (one-tailed Mann-Whitney test *P* values) are shown. **g** Western blot results showing lower Lc3-II/control signal ratios in monotherapies relative to controls. **h** Western blot

1051 results showing increased Hrh1 expression in the combinations relative to
1052 rapamycin alone, and decreased expression of S6 total in the rapamycin-
1053 loratadine combination. **i** *Prlr* expression quantification in tumors of each
1054 treatment group (n = 4-5/group). Significant differences between the groups are
1055 shown. **j** Representative images of immunohistochemical positivity of Prlr in
1056 tumors treated with rapamycin alone and rapamycin-loratadine combined. Scale
1057 bars are shown.
1058

SUPPLEMENTARY FIGURE LEGENDS

Fig. S1. *HRH1* expression associations in breast cancer. a Kaplan-Meier lung metastasis-free survival (LMFS) curves based on categorization of *HRH1* expression in breast tumors. The multivariate Cox proportional-hazards regression results are shown: HR, hazard ratio; CI, confidence interval. **b** Results from the Gene Set Enrichment Analysis (GSEA) method showing positive expression correlations (based on PCCs) between *HRH1* and key gene sets as indicated. The GSEA normalized enrichment score (NES) and association *P* values are indicated.

Fig. S2. *Aldh* and *Mao* gene expression analyses in ELT3 cells. Graph showing gene expression differences (log-fold changes) of key genes (X-axis) in *Tsc2*-deficient relative to *TSC2*-reconstituted cell counterparts. The asterisk indicates significant difference (Mann-Whitney test *P* value). Bars indicate means and SDs.

Fig. S3. Pilot *in vivo* therapeutic study in LAM using clorgyline, everolimus, GA11, and rasagiline. Graphs showing ELT3-V3 tumor growth rates under different treatment conditions as indicated in the insets. Asterisks indicate significant reduction in the response to the drug combinations relative to that of everolimus alone.

Fig. S4. ELT3 tumor cell senescence and cleaved caspase-3 analyses. Top left panel, graph showing numbers of senescent cells (as detected by β-galactosidase positivity) in ELT3 tumor groups as depicted in the X-axis. Top

right panels, representative images of β-galactosidase staining results in a control tumor, and in a rapamycin plus clorgyline-treated tumor. Bottom left panel, graph showing numbers of caspase-3-positive cells in tumor groups. Bottom right panels, western blot results for cleaved caspase-3 in tumors treated with rapamycin alone and rapamycin combinations.

Fig. S5. Gene expression changes and functional differences between ELT3 rapamycin-treated and control tumors. a Gene ontology (GO) terms significantly associated with genes up-regulated (left panel) or down-regulated (right panel) in rapamycin-treated compared with control tumors. **b** GSEA association results between mTOR-TSC2 regulated gene sets[26] and expression differences between ELT3 rapamycin-treated and control tumors. Normalized enrichment scores (NESs) and corresponding *P* values are shown.

Fig. S6. Mao and Hrh1 inhibition causes mitophagy alteration in *Tsc2*-deficient MEFs. Graph showing percentages of mitophagic cells under different conditions as indicated on the X-axis (6-hour drug treatments). Asterisk indicates significant differences relative to DMSO-treated cells (one-way ANOVA test). A mitochondrial uncoupler, carbonyl cyanide m-chlorophenylhydrazone (CCCP), was used as positive control at a concentration of 10 μM.

Fig. S7. Cell death analysis in 105K treated tumors with single drugs. Western blot results of caspase-3 in four tumors of each treatment group as indicated.

SUPPLEMENTARY TABLES

Table S1. a Genes coding for enzymes and with a significant negative correlation with *TSC2* in lung-metastatic breast cancer. **b** Quantified metabolites in plasma samples from healthy women, LAM and related pulmonary disease patients.

Table S2. Over-expressed genes in both mTOR-Mao inhibition combinations relative to rapamycin alone when treating ELT3 tumor xenografts.

Table S3. Primers used for gene expression analyses.

Figure 1

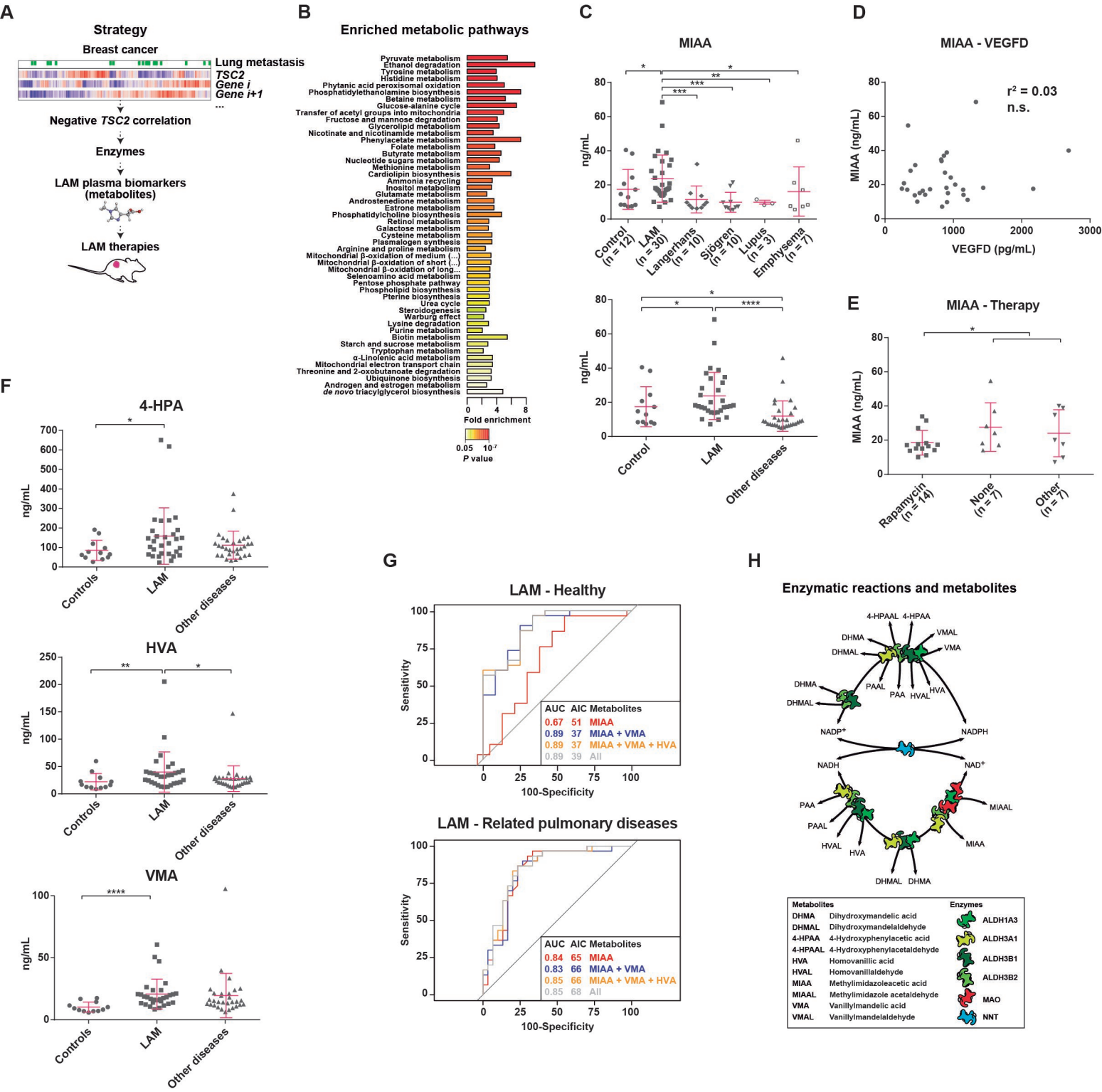
A
Strategy
Breast cancer
Lung metastasis
TSC2
Gene i
Gene i+1
...
Negative TSC2 correlation
Enzymes
LAM plasma biomarkers (metabolites)
LAM therapies
B
Enriched metabolic pathways
Pyruvate metabolism
Ethanol degradation
Tyrosine metabolism
Histidine metabolism
Phytanic acid peroxisomal oxidation
Phosphatidylethanolamine biosynthesis
Betaine metabolism
Glucose-alanine cycle
Transfer of acetyl groups into mitochondria
Fructose and mannose degradation
Glycerolipid metabolism
Nicotinate and nicotinamide metabolism
Phenylacetate metabolism
Folate metabolism
Butyrate metabolism
Nucleotide sugars metabolism
Methionine metabolism
Cardiolipin biosynthesis
Ammonia recycling
Inositol metabolism
Glutamate metabolism
Androstenedione metabolism
Estrone metabolism
Phosphatidylcholine biosynthesis
Retinol metabolism
Galactose metabolism
Cysteine metabolism
Plasmalogen synthesis
Arginine and proline metabolism
Mitochondrial β-oxidation of medium (...)
Mitochondrial β-oxidation of short (...)
Mitochondrial β-oxidation of long...
Selenoamino acid metabolism
Pentose phosphate pathway
Phospholipid biosynthesis
Pterine biosynthesis
Urea cycle
Steroidogenesis
Warburg effect
Lysine degradation
Purine metabolism
Biotin metabolism
Starch and sucrose metabolism
Tryptophan metabolism
α-Linolenic acid metabolism
Mitochondrial electron transport chain
Threonine and 2-oxobutanoate degradation
Ubiquinone biosynthesis
Androgen and estrogen metabolism
de novo triacylglycerol biosynthesis
0
4
8
Fold enrichment
0.05
10-7
P value
C
MIAA
ng/mL
Control (n = 12)
LAM (n = 30)
Langerhans (n = 10)
Sjögren (n = 10)
Lupus (n = 3)
Emphysema (n = 7)
Control
LAM
Other diseases
D
MIAA - VEGFD
r2 = 0.03
n.s.
MIAA (ng/mL)
VEGFD (pg/mL)
E
MIAA - Therapy
MIAA (ng/mL)
Rapamycin (n = 14)
None (n = 7)
Other (n = 7)
F
4-HPA
HVA
VMA
ng/mL
Controls
LAM
Other diseases
G
LAM - Healthy
Sensitivity
100-Specificity
AUC AIC Metabolites
0.67 51 MIAA
0.89 37 MIAA + VMA
0.89 37 MIAA + VMA + HVA
0.89 39 All
LAM - Related pulmonary diseases
AUC AIC Metabolites
0.84 65 MIAA
0.83 66 MIAA + VMA
0.85 66 MIAA + VMA + HVA
0.85 68 All
H
Enzymatic reactions and metabolites
4-HPAAL
4-HPA
VMAL
DHMA
DHMAL
VMA
PAAL
PAA
HVAL
HVA
NADP+
NADPH
NADH
NAD+
MIAAL
MIAA
Metabolites
DHMA Dihydroxymandelic acid
DHMAL Dihydroxymandelaldehyde
4-HPAA 4-Hydroxyphenylacetic acid
4-HPAAL 4-Hydroxyphenylacetaldehyde
HVA Homovanillic acid
HVAL Homovanillaldehyde
MIAA Methylimidazoleacetic acid
MIAAL Methylimidazole acetaldehyde
VMA Vanillylmandelic acid
VMAL Vanillylmandelaldehyde
Enzymes
ALDH1A3
ALDH3A1
ALDH3B1
ALDH3B2
MAO
NNT

Figure 2

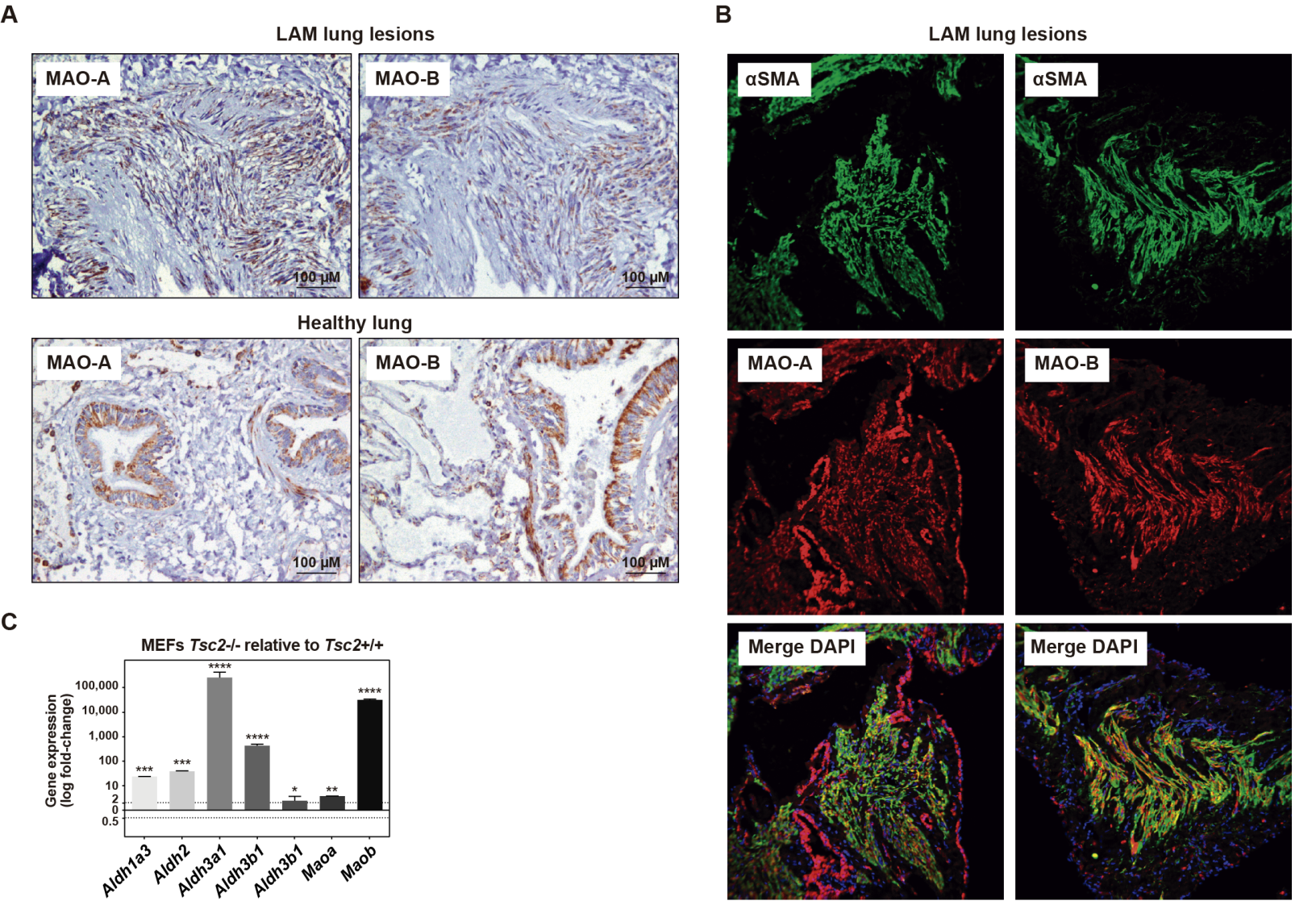
A
LAM lung lesions
MAO-A
MAO-B
100 µM
Healthy lung
B
LAM lung lesions
αSMA
MAO-A
MAO-B
Merge DAPI
C
MEFs Tsc2-/- relative to Tsc2+/+
Gene expression (log fold-change)
100,000
10,000
1,000
100
10
2
0
0.5
Aldh1a3
Aldh2
Aldh3a1
Aldh3b1
Aldh3b1
Maoa
Maob
D
MEFs
Tsc2+/+
Tsc2-/-
DMSO
Everolimus
Tsc2
Aldh2
pS6
Total S6
Tubulin
Mao-A
Mao-B
Actin
E
MEF Tsc2+/+
0.00%
MEF Tsc2-/-
0.19%
Side scatter
ALDH activity
(green fluorescent)
F
Mao activity (CPM/µg protein)
MEF
Tsc2 +/+
Tsc2-/-
Control
1 µM deprenyl
1 µM clorgyline
1 µM deprenyl + 1 µM clorgyline
G
FAD (pmol)

Figure 3

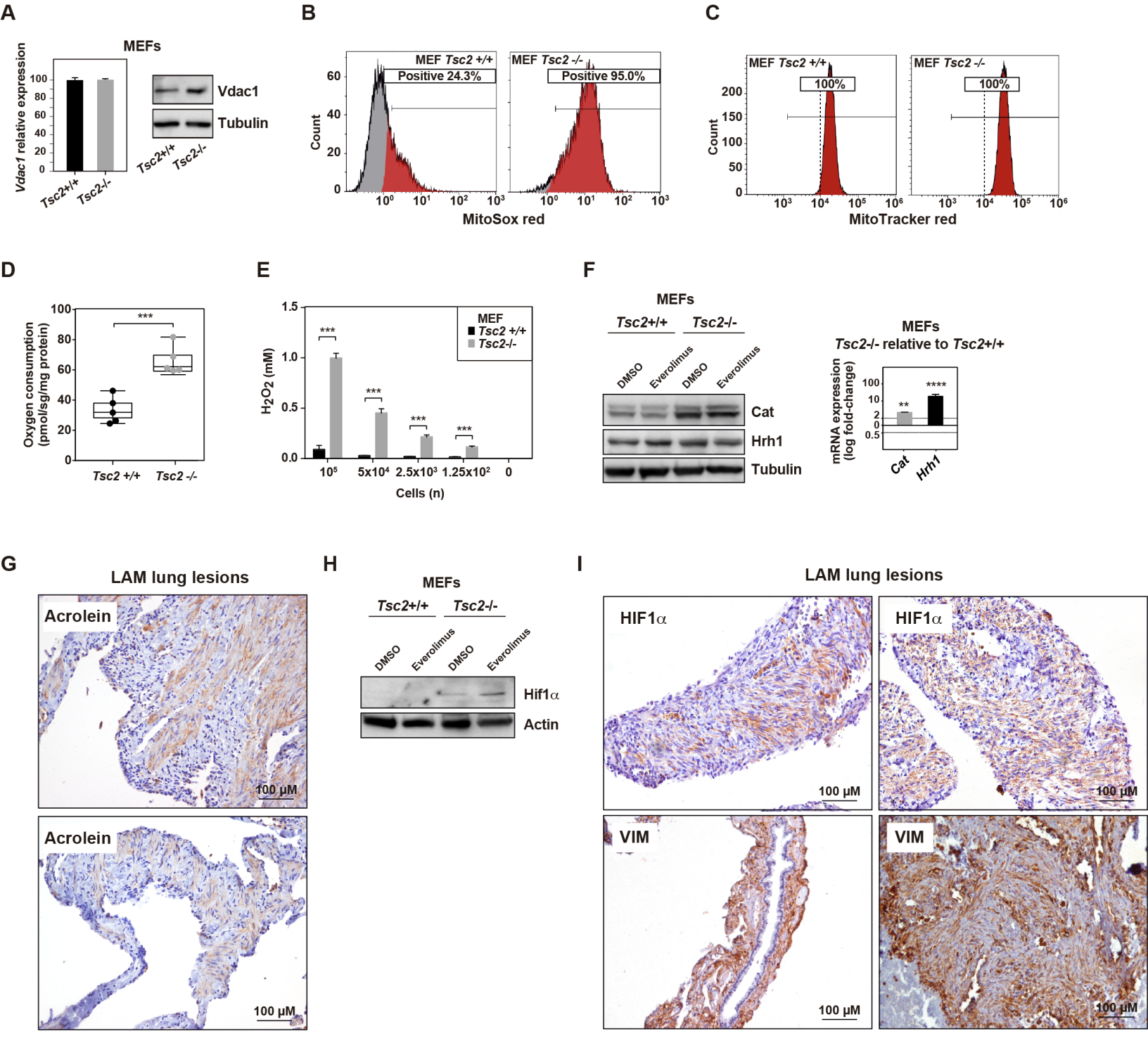
A
MEFs
Vdac1 relative expression
Tsc2+/+
Tsc2-/-
Vdac1
Tubulin
B
MEF Tsc2 +/+
Positive 24.3%
MEF Tsc2 -/-
Positive 95.0%
Count
MitoSox red
C
MEF Tsc2 +/+
100%
MEF Tsc2 -/-
100%
Count
MitoTracker red
D
Oxygen consumption (pmol/sg/mg protein)
Tsc2 +/+
Tsc2 -/-
E
MEF
Tsc2 +/+
Tsc2-/-
H2O2 (mM)
Cells (n)
F
MEFs
Tsc2+/+
Tsc2-/-
DMSO
Everolimus
Cat
Hrh1
Tubulin
MEFs
Tsc2-/- relative to Tsc2+/+
mRNA expression (log fold-change)
G
LAM lung lesions
Acrolein
100 µM
H
MEFs
Hif1α
Actin
I
LAM lung lesions
HIF1α
VIM
100 µM

Figure 4

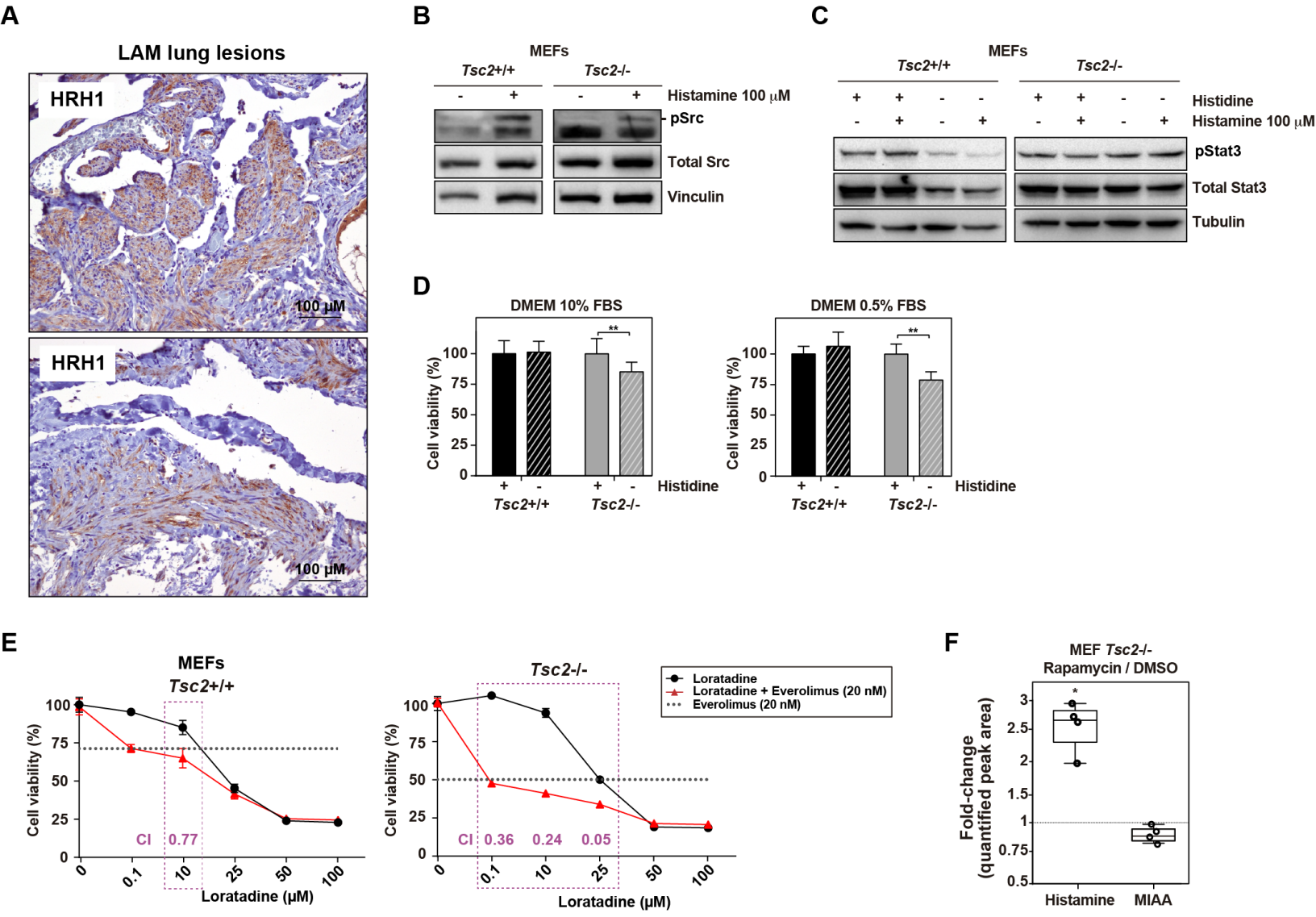
A
LAM lung lesions
HRH1
100 µM
HRH1
100 µM
B
MEFs
Tsc2+/+
Tsc2-/-
Histamine 100 µM
pSrc
Total Src
Vinculin
C
MEFs
Tsc2+/+
Tsc2-/-
Histidine
Histamine 100 µM
pStat3
Total Stat3
Tubulin
D
DMEM 10% FBS
DMEM 0.5% FBS
Cell viability (%)
Histidine
Tsc2+/+
Tsc2-/-
E
MEFs
Tsc2+/+
Tsc2-/-
Loratadine
Loratadine + Everolimus (20 nM)
Everolimus (20 nM)
Cell viability (%)
CI 0.77
CI 0.36 0.24 0.05
Loratadine (µM)
F
MEF Tsc2-/-
Rapamycin / DMSO
Fold-change (quantified peak area)
Histamine
MIAA

Figure 5

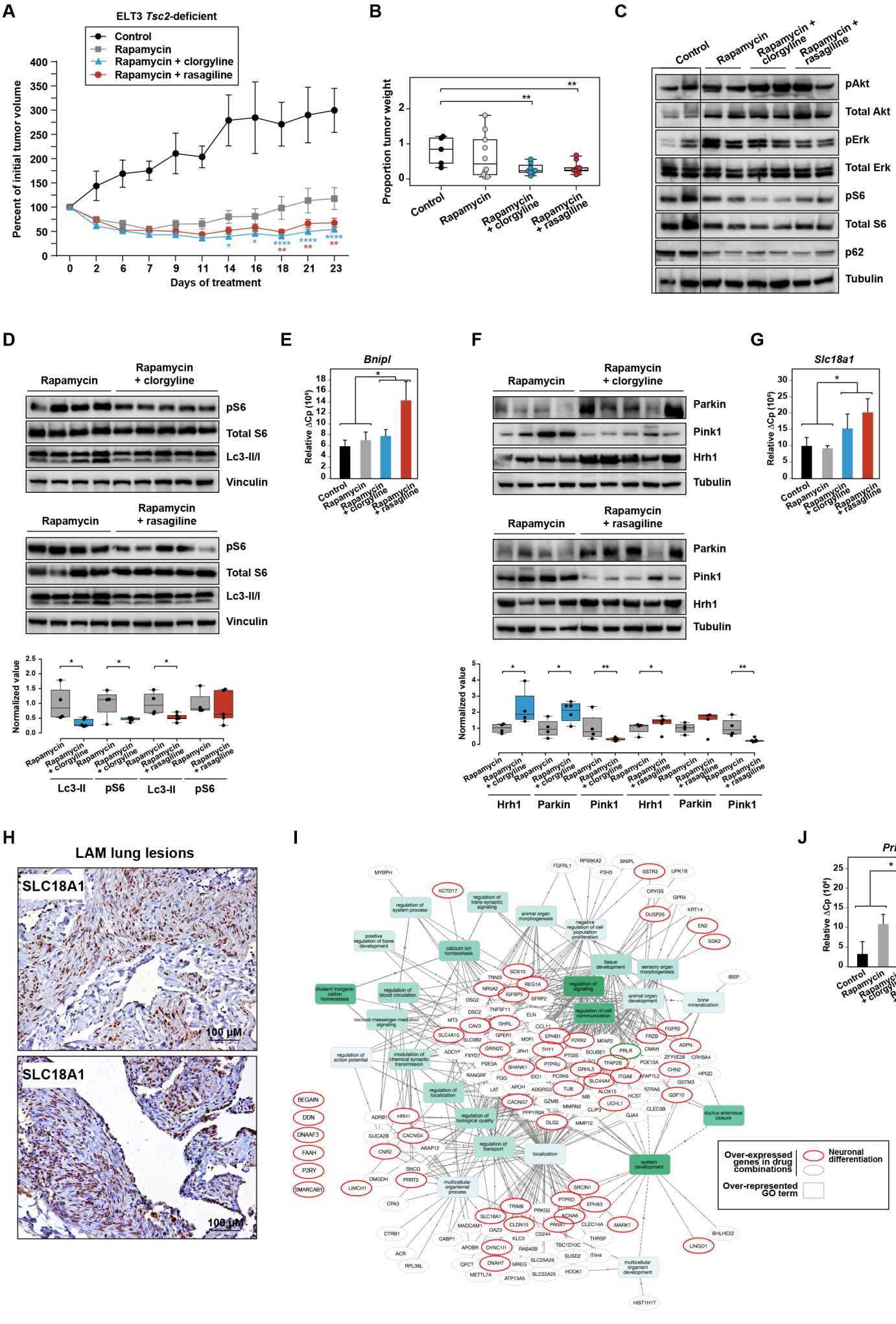
A
ELT3 Tsc2-deficient
Control
Rapamycin
Rapamycin + clorgyline
Rapamycin + rasagiline
Percent of initial tumor volume
Days of treatment
B
Proportion tumor weight
Control
Rapamycin
Rapamycin + clorgyline
Rapamycin + rasagiline
C
Control
Rapamycin
Rapamycin + clorgyline
Rapamycin + rasagiline
pAkt
Total Akt
pErk
Total Erk
pS6
Total S6
p62
Tubulin
D
Rapamycin
Rapamycin + clorgyline
pS6
Total S6
Lc3-II/I
Vinculin
Rapamycin
Rapamycin + rasagiline
pS6
Total S6
Lc3-II/I
Vinculin
Normalized value
Lc3-II
pS6
Lc3-II
pS6
E
Bnipl
Relative ΔCp (10⁶)
Control
Rapamycin
Rapamycin + clorgyline
Rapamycin + rasagiline
F
Rapamycin
Rapamycin + clorgyline
Parkin
Pink1
Hrh1
Tubulin
Rapamycin
Rapamycin + rasagiline
Parkin
Pink1
Hrh1
Tubulin
Normalized value
Hrh1
Parkin
Pink1
Hrh1
Parkin
Pink1
G
Slc18a1
Relative ΔCp (10⁶)
Control
Rapamycin
Rapamycin + clorgyline
Rapamycin + rasagiline
H
LAM lung lesions
SLC18A1
100 μM
SLC18A1
100 μM
I
BEGAIN
DDN
DNAAF3
FAAH
P2RY
SMARCAB1
Over-expressed genes in drug combinations
Neuronal differentiation
Over-represented GO term
J
Prlr
Relative ΔCp (10⁶)
Control
Rapamycin
Rapamycin + clorgyline
Rapamycin + rasagiline

Figure 6

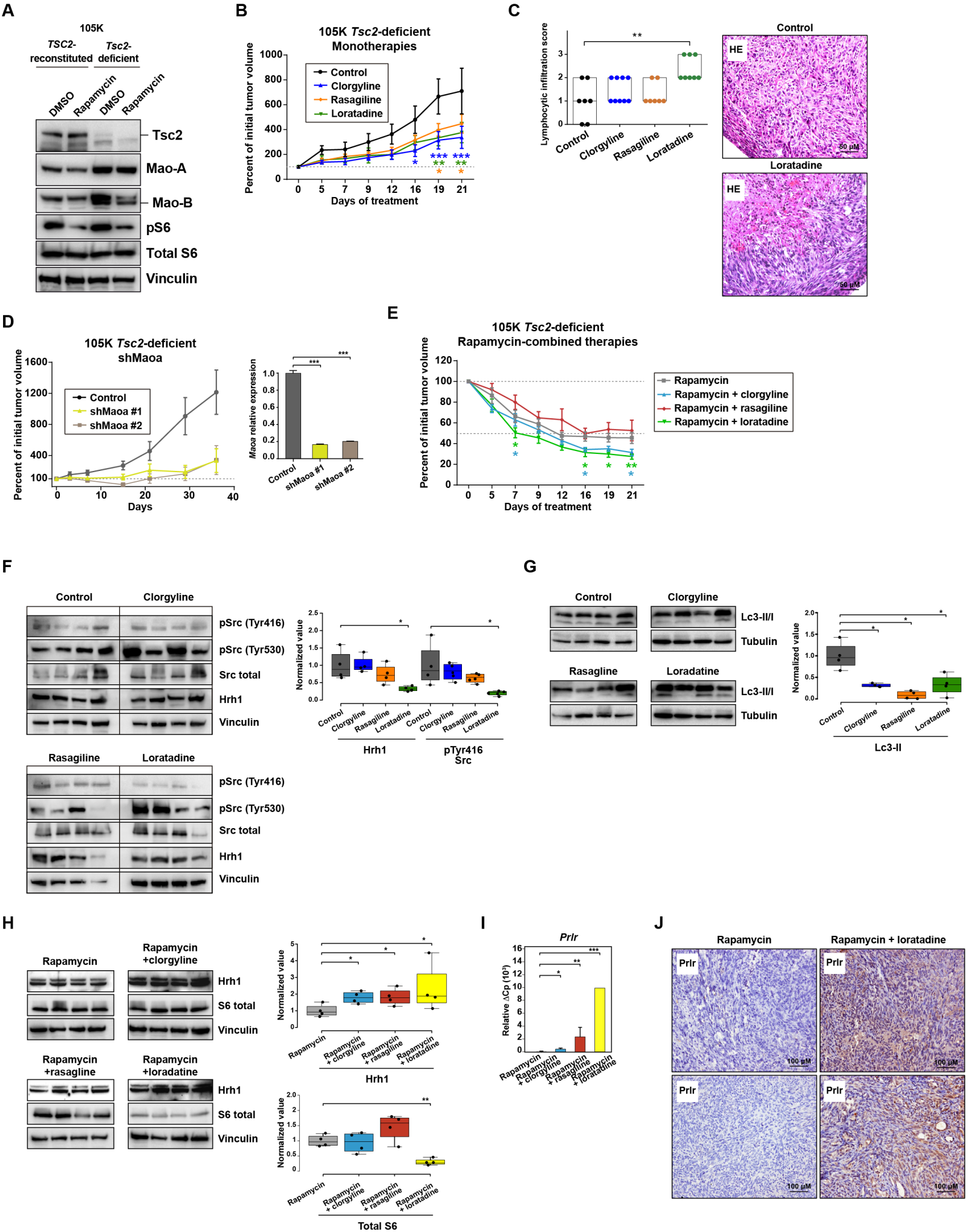
A
105K
TSC2-reconstituted
Tsc2-deficient
DMSO
Rapamycin
DMSO
Rapamycin
Tsc2
Mao-A
Mao-B
pS6
Total S6
Vinculin
B
105K Tsc2-deficient Monotherapies
Percent of initial tumor volume
Control
Clorgyline
Rasagiline
Loratadine
Days of treatment
C
Lymphocytic infiltration score
Control
Clorgyline
Rasagiline
Loratadine
HE
50 µM
D
105K Tsc2-deficient shMaoa
Percent of initial tumor volume
Control
shMaoa #1
shMaoa #2
Days
Maoa relative expression
E
105K Tsc2-deficient Rapamycin-combined therapies
Percent of initial tumor volume
Rapamycin
Rapamycin + clorgyline
Rapamycin + rasagiline
Rapamycin + loratadine
Days of treatment
F
Control
Clorgyline
Rasagiline
Loratadine
pSrc (Tyr416)
pSrc (Tyr530)
Src total
Hrh1
Vinculin
Normalized value
Hrh1
pTyr416 Src
G
Lc3-II/I
Tubulin
Lc3-II
H
Rapamycin
Rapamycin +clorgyline
Rapamycin +rasagline
Rapamycin +loradatine
Hrh1
S6 total
Vinculin
Total S6
I
Prlr
Relative ΔCp (10³)
J
Rapamycin
Rapamycin + loratadine
Prlr
100 µM